Mössbauer Effect in $K_3Fe(CN)_6$†

W. T. OOSTERHUIS
Physics Department, Carnegie-Mellon University, Pittsburgh, Pennsylvania and Nuclear Physics Division, Atomic Energy Research Establishment, Harwell, England

AND

GEORGE LANG
Nuclear Physics Division, Atomic Energy Research Establishment, Harwell, England

(Received 24 July 1968)

A Mössbauer-effect study of the low-spin compound $K_3Fe(CN)_6$ has been carried out under a wide variety of conditions. In concentrated samples, the quadrupole splitting, linewidth, and isomer shift were measured as a function of temperature. The components of the electric-field-gradient tensor (EFG) were determined from the quadrupole peak area ratios of single-crystal absorbers at 20 and 300°K. The orientations of the g tensor and EFG in the concentrated salt were also determined by experiments using large magnetic fields in single crystals at low temperatures. Paramagnetic hyperfine structure was found at low temperatures in samples of $K_3Fe(CN)_6$ diluted in the diamagnetic $K_3Co(CN)_6$. The theory of hyperfine interactions as applied to this case is reviewed, and the sensitivity of the Mössbauer spectrum to the relative directions of the g tensor and cubic field are discussed. Spectra are calculated using two models based on ESR and susceptibility results, and one of these is found to be in good agreement with the data.

1. INTRODUCTION

POTASSIUM ferricyanide is a compound in which strong covalent bonding exists between a metallic ion and its ligands. The ferricyanide complex has only one unpaired electron and a spin of $\frac{1}{2}$ compared to the more usual $S=\frac{5}{2}$ configuration for a ferric ion. As a prototypal material, it has received a large amount of experimental attention and thus is an attractive candidate for Mössbauer studies. An additional motivation for looking at the Mössbauer spectrum was an anomaly in the specific heat at 130°K,[1] as well as some strange behavior in the magnetic susceptibility at this temperature.[2] Although the entropy associated with this anomaly appeared to be less than that needed for a magnetic phase transition, it was thought worth while to look for magnetic splitting in the Mössbauer pattern below 130°K. The results of this measurement were negative apart from a broadening of the absorption lines at low temperature which was probably due to an increased spin-lattice relaxation time.

The possibility of studying the paramagnetic hyperfine structure in the Mössbauer spectrum thus presented itself. Use of magnetically dilute Fe^{57} enriched specimens provided its realization, and much of the present paper is devoted to the description of the observed magnetic hyperfine spectra. The theory of ESR hyperfine interactions, somewhat modified and extended, provides a satisfactory interpretation of the experiments.

The Mössbauer spectrum of powdered absorbers of $K_3Fe(CN)_6$ was first studied by Kerler and Neuwirth[3] in the temperature range of 150–330°K. Golding's calculation[4] of the temperature dependence of the quadrupole splitting seemed to explain their results. We have extended these measurements to liquid-helium temperatures[5] and found behavior that contrasts with Golding's theory and also with a calculation using the formalism of Ingalls.[6]

In 1956, Baker, Bleaney, and Bowers[7] measured the principal axes of the g tensor and found that there were two similar iron sites in the crystal, with g tensors which were differently oriented. They also found that the principal axes of the g tensors did not coincide with the cubic axes of the ferricyanide octahedra but were rotated about one of the cubic axes by an angle $\gamma=45°$. Bleaney and O'Brien[8] then fitted the g-tensor data with a set of wave functions for the ground-state Kramers doublet and proceeded to calculate the temperature-dependent susceptibilities in the single crystal from these wave functions. By fitting the temperature dependence of the susceptibilities they were able to determine the separation of the electronic energy levels, and were also quite successful in explaining the anisotropy of the susceptibility tensor.

We will see below that the wave functions and energy levels which fit the magnetic data so well are also, with certain reservations, consistent with the paramagnetic Mössbauer spectra. We might note that no hyperfine structure was observed by the ESR workers because of the small amount of Fe^{57} in their samples and also because of the very broad absorption line in $K_3Fe(CN)_6$.

† Supported by the National Science Foundation and the Office of Naval Research.

[1] C. C. Stephenson and J. C. Morrow, J. Am. Chem. Soc. **78**, 275 (1956).

[2] G. Shoffa, O. Ristan, and K. Ruckpaul, Zh. Experim. i Teor. Fiz. **35**, 641 (1958) [English transl.: Soviet Physics.—JETP **8**, 445 (1959)].

[3] W. Kerler and W. Neuwirth, Z. Physik **167**, 188 (1962).

[4] R. M. Golding, Mol. Phys. **12**, 13 (1967).

[5] W. Oosterhuis, G. Lang, and S. Debenedetti, Phys. Letters **24**, 346 (1967).

[6] R. I. Ingalls, Phys. Rev. **133**, A787 (1964).

[7] J. M. Baker, B. Bleaney, and K. D. Bowers, Proc. Phys. Soc. (London) **B69**, 1205 (1956).

[8] B. Bleaney and M. C. M. O'Brien, Proc. Phys. Soc. (London) **B69**, 1216 (1956).

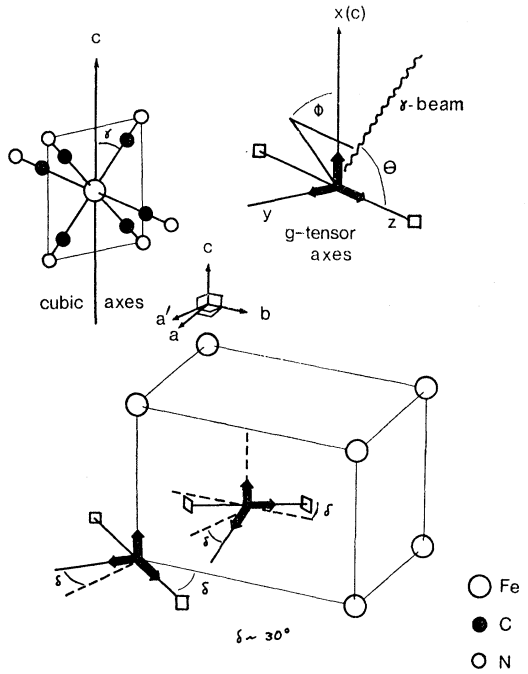

FIG. 1. Structure of $K_3Fe(CN)_6$ showing the orientations of the ligand (cubic) axes and g-tensor axes (x,y,z) with respect to the crystalline axes $(a,b\ c)$.

The crystalline structure of $K_3Fe(CN)_6$ has been the subject of controversy[9] which has only recently been resolved by the discovery that $K_3Fe(CN)_6$ grows in polytypes as does the isomorphic salt $K_3Co(CN)_6$.[10]

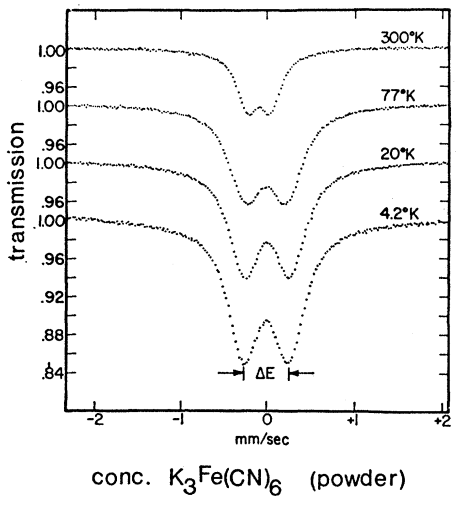

FIG. 2. Mössbauer spectra of concentrated $K_3Fe(CN)_6$ (powder) at 300, 77, 20, and 4.2°K.

A basic unit of structure is drawn in Fig. 1, which shows the positions of the iron sites and their orientations with respect to the crystal axes. One site is the cell corner. The other, in the center of the b-c face, is related to the corner site by a glide plane reflection. This is the unit cell of the monoclinic polytype. The fact that there are two differently oriented sites in the crystal has significance in single-crystal work only.

In order to visualize the polytypism, let the unit of Fig. 1 be called A type and let the unit which is obtained by rotation of A through 180° about the c axis be called B type. The normal crystal has only A-type cells. Then consider an arrangement in which alternate sheets of A and B types lie in planes normal to a'. The actual unit cell is then orthorhombic and has twice the volume of A. Other sequences of A and B are possible, giving rise to a variety of polytypes. The immediate or octahedral environment of the iron nuclei is not affected by polytypism, but it is possible that the lower symmetry components are. In the ESR spectra of $K_3Cr(CN)_6$,[10] however, polytypism affects the energy splittings by only a few tenths of a percent, while in $K_3Fe(CN)_6$ it has been detected only through small

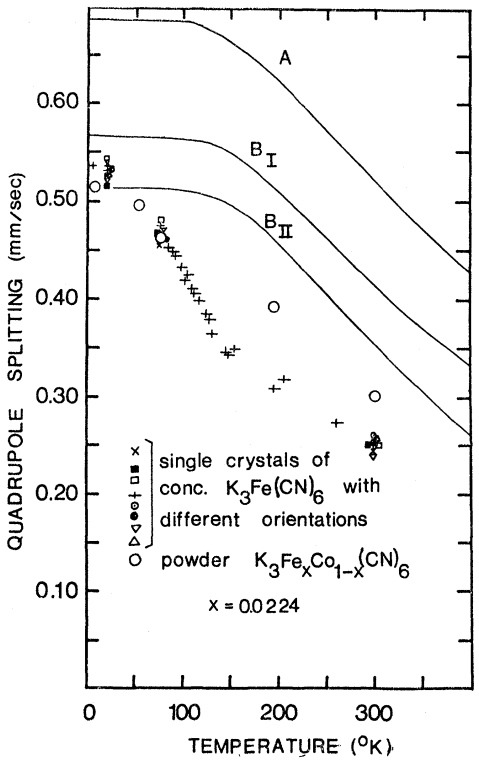

FIG. 3. Temperature dependence of the quadrupole splitting in $K_3Fe(CN)_6$. The experiments were done with single crystals of $K_3Fe(CN)_6$ with various orientations with respect to the γ beam and one powder sample of Fe diluted in $K_3Co(CN)_6$. The solid lines are A splitting calculated with models I and II and no lattice EFG included, B_I=splitting calculated with model I including the lattice EFG (Table IV, column 2), B_{II}=splitting calculated with model II including the lattice EFG (Table IV, column 2).

[9] C. Gottfried and J. G. Nagleschmidt, Z. Krist. **73**, 357 (1930); V. Barkhatov and H. Zhadanov, Acta Physicochim. URSS **16**, 43 (1942); Y. Okaya *et al.*, Acta Cryst. **10**, 798 (1957).

[10] N. A. Curry and W. A. Runciman, Acta Cryst. **12**, 674 (1959); J. A. Kohn and W. D. Townes, *ibid.* **14**, 617 (1961); J. O. Artman, J. C. Murphy, J. A. Kohn, and W. D. Townes, Phys. Rev. Letters **4**, 607 (1960).

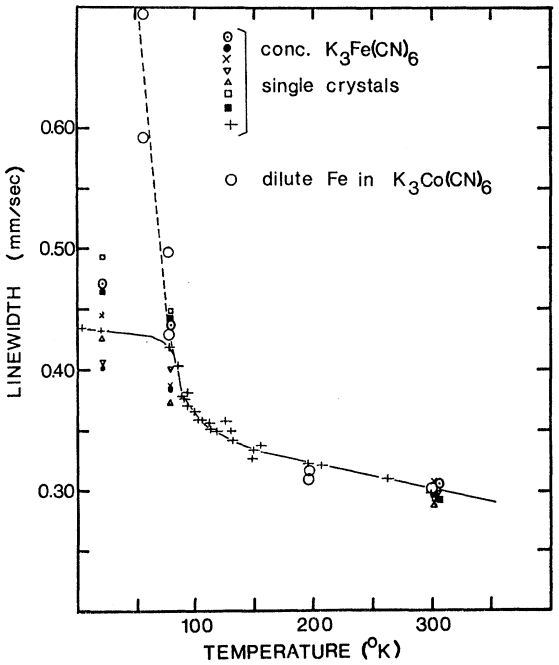

FIG. 4. Temperature dependence of the linewidth (full width at half-maximum) in single crystals of $K_3Fe(CN)_6$ (with various orientations) and also in a dilute (2.24% Fe) sample. Variation in sample thickness probably causes the scatter in the experimental linewidth. In the dilute sample, the two quadrupole peaks are found to have different linewidths at a given temperature due to relaxation effects.

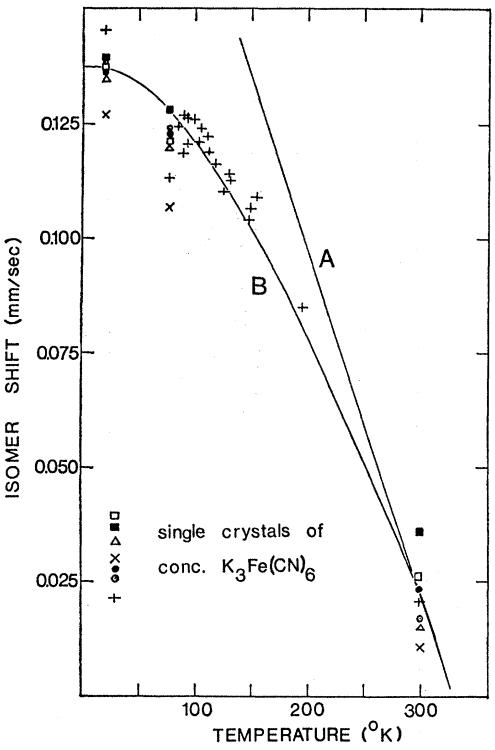

FIG. 5. The temperature dependence of the isomer shift in single crystals of $K_3Fe(CN)_6$. The straight line A is predicted from the classical Dulong and Petit law, while the curved line B results from numerical integration of the specific heat (Ref. 1) and has zero slope at 0°K due to quantum effects.

effects upon the NMR spectrum of C^{13}.[11] Thus we may assume that the Mössbauer spectra of the ferricyanide will be insensitive to polytypism.

2. EXPERIMENTAL TECHNIQUES

These measurements were made on a constant acceleration Mössbauer spectrometer of the usual type in connection with a multichannel analyzer driven in the time mode.[12] The small transverse magnetic fields were produced by a permanent magnet of about 500 G at the center of the pole gap, and the longitudinal fields were produced by trapping flux within lead washers concentric with the sample in a Helmholtz type of arrangement at 4.2°K. This gave a longitudinal field strength of about 100 G, less than the critical field of Pb at 4.2°K. Also a pair of 200-turn Helmholtz coils were wound with a diameter of 3 in. to produce the very small longitudinal fields up to 30 G. For very high fields, a superconducting solenoid was used.

The powder absorbers of $K_3Fe(CN)_6$ were made of crushed microcrystals which were grown from a water solution of commercially available $K_3Fe(CN)_6$. Single crystals of the ferricyanide were easily grown from a saturated water solution. Slices 0.010-in. thick (corresponding to an effective thickness of 3.5) were made

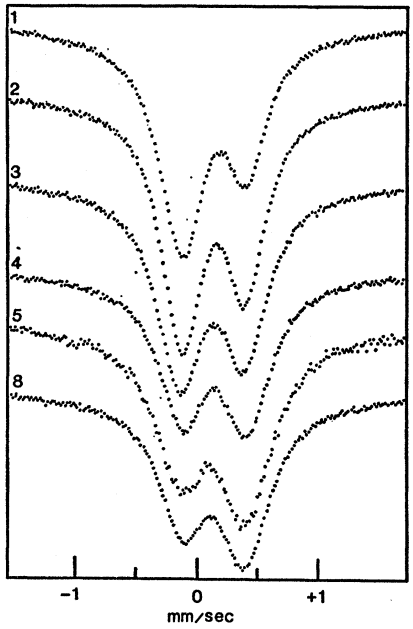

FIG. 6. Some single-crystal Mössbauer spectra in $K_3Fe(CN)_6$ at 20°K in zero external field. The different spectra represent different orientations of the crystal with respect to the γ beam. The spectra can be identified by their numbers which are those of Table III.

[11] D. Davis and R. J. Kurland, J. Chem. Phys. 46, 388 (1967).
[12] T. E. Cranshaw, Nucl. Instr. Methods 30, 101 (1964).

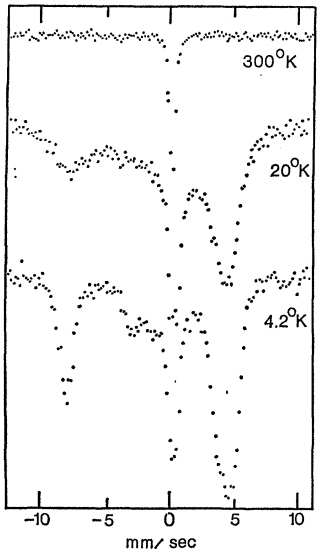

FIG. 7. A dilute sample of $K_3Fe_xCo_{1-x}(CN)_6$ for $x=0.0224$ showing the effect of temperature on the Mössbauer spectrum through spin-lattice relaxation.

using a string saw. Variations in thickness may account for the scatter in the linewidth observed in these samples. $K_3Fe(CN)_6$ enriched in Fe^{57} was prepared from Fe_2O_3 by a procedure given to the authors by Epstein.[13] The enriched (80% Fe^{57}) ferricyanide was diluted in solutions of $K_3Co(CN)_6$, and microcrystals were then grown from these saturated solutions and ground into a fine powder. The ferricyanide concentration of each sample was determined by optical absorption of the $K_3Fe(CN)_6$ complex at 414 nm.[14] The samples of $K_3Fe(CN)_6$ freshly dissolved in glycerine were frozen into a glass. All diluted samples were weighed out to include 0.22 ± 0.02 mg Fe^{57}/cm^2.

The Mössbauer source was Co^{57} in chromium and was run at 300°K. The spectra were all calibrated with respect to an iron metal absorber,[15] with zero velocity taken as the centroid of the iron spectrum.

The absorbers were cooled in conventional Dewars, whereby the absorber was placed in thermal contact with the refrigerant through a copper sample holder, or else immersed in the coolant itself. For some of the variable temperature measurements, the temperature was measured by means of a carbon resistance which was calibrated at 4.2, 20, 77, and 300°K.

The experimental data were normalized and corrected for solid angle effects by least-squares fitting of a quadratic polynomial to a blank run (background) and then dividing the experimental data by the polynomial. For the spectra with only quadrupole splitting, the two absorption peaks were fitted to two Lorentzian lines to determine the intensities, line positions, and linewidths, also by the least-squares method.

3. EXPERIMENTAL RESULTS

In this section, we present the results of a series of experiments, using the Mössbauer effect in the ferricyanide complex under varying conditions of temperature, concentration, and magnetic field.

In Fig. 2 are examples of spectra of a powder sample of undiluted $K_3Fe(CN)_6$ at various temperatures. These and other (single-crystal) spectra were fitted to Lorentzian line shapes to determine the quadrupole splitting, linewidth, isomer shift, and peak intensities (Figs. 3, 4, 5 and Table III). The quadrupole splitting is quite temperature-dependent as shown in Fig. 3. The linewidth of the absorption peaks also depends upon the temperature as seen in Fig. 4. The scatter in linewidths of different samples is probably due to variations in sample thickness. Temperatures in the range 80 to 195°K are known to an accuracy of ±5°K because of the insensitivity of a carbon resistance thermometer above 20°K. Data for a diluted sample K_3Fe_x,

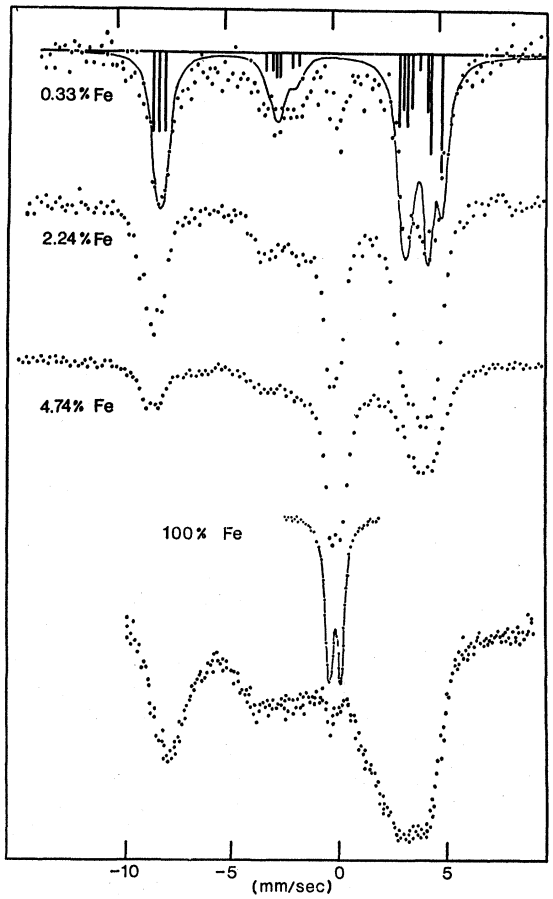

FIG. 8. $K_3Fe(CN)_6$ at 4.2°K showing the effects of dilution on the Mössbauer spectrum through spin-spin relaxation. The bottom spectrum is $K_3Fe(CN)_6$ dissolved in gylcerine. The solid curve is a calculation done with model II.

[13] L. Epstein (private communication).
[14] A. V. Kiss, J. Abraham, and I. Hegedus, Z. Anorg. Allgem. Chem. 244, 98 (1940).
[15] R. S. Preston, S. S. Hanna, and J. Herberle, Phys. Rev. 128, 2207 (1962).

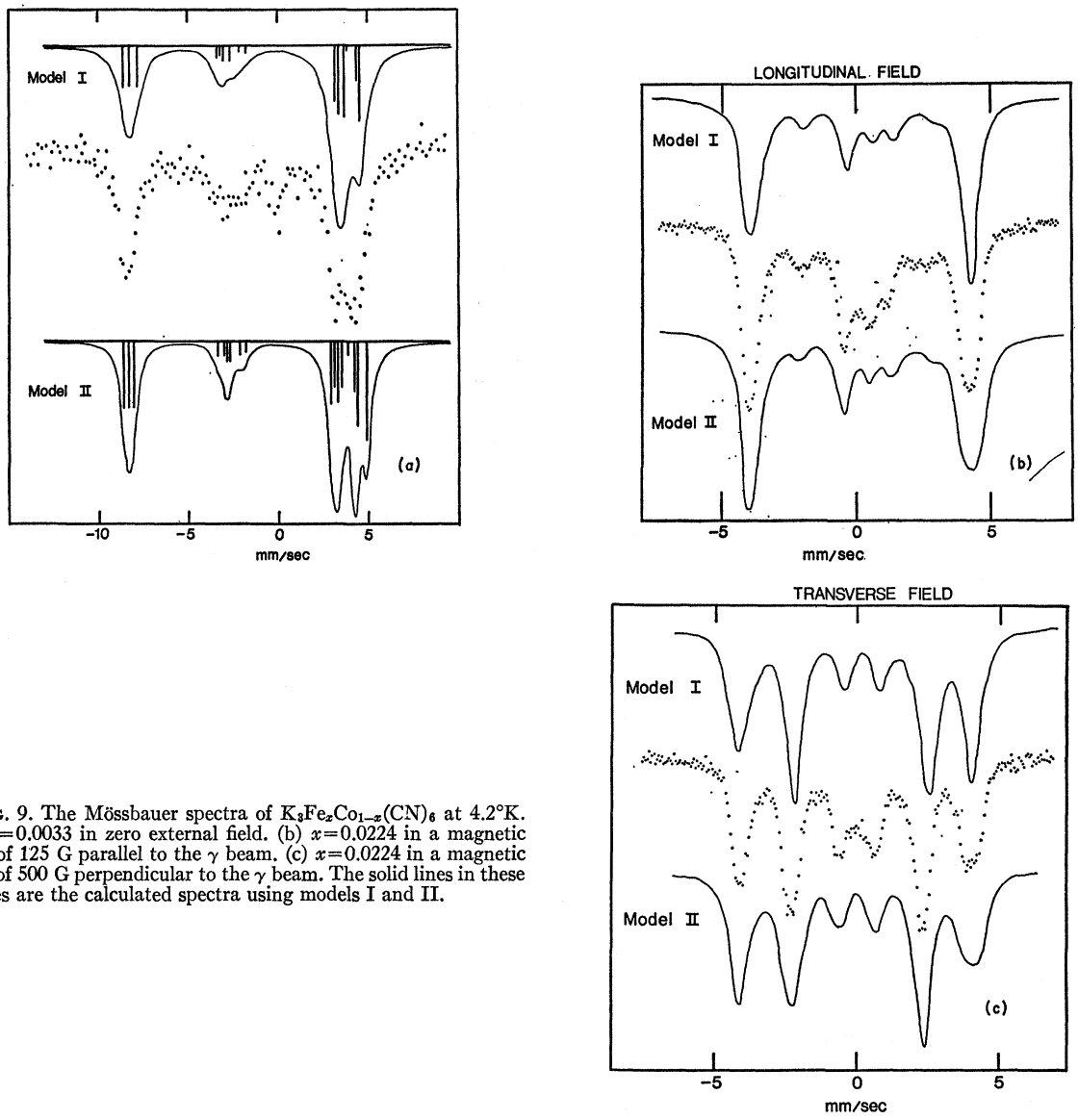

FIG. 9. The Mössbauer spectra of $K_3Fe_xCo_{1-x}(CN)_6$ at 4.2°K. (a) $x=0.0033$ in zero external field. (b) $x=0.0224$ in a magnetic field of 125 G parallel to the γ beam. (c) $x=0.0224$ in a magnetic field of 500 G perpendicular to the γ beam. The solid lines in these figures are the calculated spectra using models I and II.

$Co_{1-x}(CN)_6$ are plotted in Figs. 3 and 4, and have somewhat different behavior from the concentrated salt. The temperature dependence of the isomer shift is shown in Fig. 5.

In Fig. 6 are shown the single-crystal Mössbauer spectra of $K_3Fe(CN)_6$ at 20°K as a function of orientation of the incident γ beam relative to the crystal axes. These spectra were also fitted to determine the quadrupole splitting, linewidth, and area ratios as a function of orientation, and the variation of the area ratio with orientation is shown in Table III. It was found that the area ratio was quite temperature-dependent in certain directions.

Figure 7 shows the variation with temperature in the Mössbauer spectra of a powder sample of $K_3Fe(CN)_6$ diluted in isomorphic, diamagnetic $K_3Co(CN)_6$. Observation of the paramagnetic hyperfine spectrum requires low temperatures to inhibit the spin-lattice relaxation and low Fe concentration to reduce the spin-spin relaxation. In Fig. 8, we show the concentration dependence of the paramagnetic hyperfine spectra at 4.2°K. The bottom spectrum of Fig. 8 is of $K_3Fe(CN)_6$ dissolved in glycerine, which forms a glass upon freezing. It is seen that this spectrum is rather similar to those of the dilute powder but has much broader lines.

Figure 9 shows the Mössbauer spectra of diluted powder $K_3Fe,Co(CN)_6$ in zero field and in moderate magnetic fields (about 400 G) with orientations parallel and perpendicular to the γ beam. Figure 10 shows the behavior of the spectrum as the strength of the longitudinal field is varied. Note the absorption lines which shift into the wings and lose their intensity as H in-

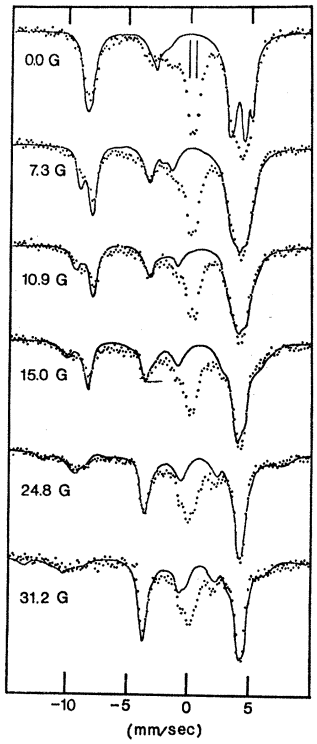

FIG. 10. Mössbauer spectra of $K_3Fe_xCo_{1-x}(CN)_6$ with $x=0.0224$ at 4.2°K showing the effects of small magnetic fields in decoupling the nuclear and electronic moments. The solid curves are calculated using model II.

creases. In Fig. 11 are the Mössbauer spectra of single crystals of $K_3Fe(CN)_6$ at low temperature with 29 kG applied along the crystal a', b, and c axes. Because the spins relax rapidly in these magnetically concentrated specimens, the magnetic hyperfine splitting depends upon the net magnetization. The quadrupole shift is seen to be largest and negative for $H_{a'}$.

4. THEORETICAL CONSIDERATIONS

A. Electronic Model for $K_3Fe(CN)_6$

Three different approaches have been used to treat the problem of the electrons in a molecular complex. Historically, the first was Pauling's method of directed valence[16] in which the ion in question is attached to its neighbors by means of hybridized electron pair bonds, each bond containing one electron from the central ion and another from the ligand.

The second method is crystal-field theory[17] which has been very successful when applied to ionic salts. Here the electron wave functions are localized on the central ion, and the interaction with the ligands is represented by a static potential which reflects the symmetry of the local environment.

[16] L. Pauling, J. Am. Chem. Soc. **53**, 1367 (1931).
[17] W. G. Penney and R. Schlapp, Phys. Rev. **41**, 194 (1932).

A third and more accurate way of writing the wave functions is to acknowledge the fact that there is some degree of covalency in any complex. This means that there are shared electrons which do not belong to any particular ion or atom, although it is often convenient to think of them as having come from a particular donor. These molecular orbital wave functions are usually represented as linear combinations of atomic orbitals and have the symmetry of the complex. Because of the strong interaction between Fe and CN, a proper treatment of potassium ferricyanide requires the molecular orbital method. For convenience, however, it is often useful to proceed with a crystal-field type of calculation, taking account of covalency through the inclusion of certain correction factors in the matrix elements. This will become clear below.

In Fig. 12, we show a partial energy level diagram of the ferricyanide complex. Only the 3d electrons of the Fe are included, together with the ligand orbitals which interact strongly with them. To the left are shown the 3d d_ϵ and d_γ wave functions of an iron ion in an octahedral field, and on the right are shown the π and σ bonding and the π^* antibonding wave functions which arise from the interaction of the $2p$ electrons of C and N. The σ^* antibonding function is not shown, but would lie somewhere high at the right in the figure. In the combined fields of Fe and CN, the approximate energy eigenstates are the molecular orbitals shown in the center of the figure. Each molecular orbital can be written as $\psi=N(\psi_{Fe}+A_\pi\psi_{CN})$, where ψ_{CN} is a linear combination of ligand orbitals constructed so as to have the same symmetry as ψ_{Fe}, the central ion wave function.

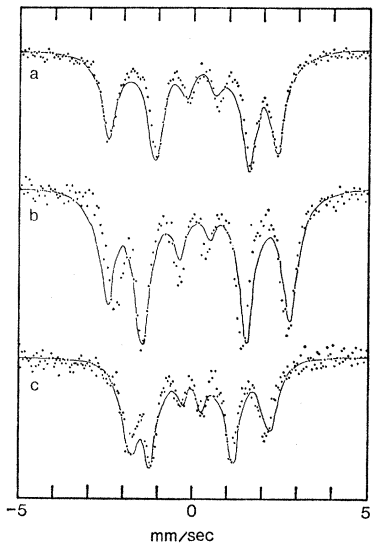

FIG. 11. Mössbauer spectra of single-crystal $K_3Fe(CN)_6$ in large magnetic fields at low temperatures. Solid curves are calculations from model II. (a) $H=29$ kg along the a axis, $T=4.2$°K, γ's directed along the c axis. (b) $H=29$ kg along the b axis, $T=4.2$°K, γ's directed along the c axis. (c) $H=29$ kg along the c axis, $T=1.7$°K, γ's directed along the a' axis.

Roughly speaking, N^2 is the fraction of time an electron in such an orbital spends on the central ion. If we think in terms of starting from a situation in which there are five 3d electrons on the iron, then all the electrons in σ^b and π^b may be regarded as having come from the ligands. Since they are now partly on the iron, this represents a donation of electrons from ligand to iron. On the other hand, the electrons in $\pi(d_\epsilon)$ have come from the iron, but are now partly on the ligand, representing a so-called back-donation to the ligands. The interaction of the state π^* is thought to enhance this back-donation considerably.[18] Proper attention to electron husbandry would require us to draw a number of additional levels to accommodate the many ligand p electrons which seem to have wandered out of the picture. These combinations do not have the necessary symmetry to interact with d_ϵ or d_γ, and have been omitted for clarity. The energy of electron-electron repulsion, which causes parallel electron spin states to be favored (Hund's first rule), is not shown in Fig. 12. In an ionic salt this would result in the promotion of two of the electrons in $\pi(d_\epsilon)$ to higher orbitals, the reduced repulsion energy of five unpaired spins making this energetically favorable. However, it is a characteristic of covalent materials, for which the ferricyanides are the prototypes, that the higher orbitals are so high that the promotion does not take place. The cubic field splitting $10Dq$ is typically 10 000 cm^{-1} in hydrated ferric salts (high spin, ionic); in ferricyanide it is about 35 000 cm^{-1}. The five electrons and the sole unpaired spin thus remain in the state labelled $\pi(d_\epsilon)$ in the figure.

We now focus our attention upon the electrons in the $\pi(d_\epsilon)$. The wave functions have the *symmetry* of the original d_ϵ orbitals, so that any matrix element which is calculated using the d_ϵ as a basis set will be proportional to the corresponding element within the actual $\pi(d_\epsilon)$ set of molecular orbitals.

We will therefore proceed with a crystal-field calculation using the d_ϵ states and take account of the covalency by the introduction of appropriate scaling factors. The treatment which follows is based upon the work of Howard[19] and of Bleaney and O'Brien,[8] extended to the prediction of Mössbauer spectra in a variety of situations.

We begin with an ion which has cubic symmetry and degenerate electronic orbitals ($|x'y'\rangle$, $|x',z'\rangle$, $|y',z'\rangle$) which reflect this symmetry. The degeneracy is lifted by placing the complex in a noncubic environment or by a Jahn-Teller distortion. We will treat this as a crystal field acting on the orbitals and solve the problem of a crystal field combined with a spin-orbit interaction.

Because the cubic crystal-field splitting is so great in comparison with both kT and the spin-orbit interaction, it is a good approximation to treat the d_ϵ electrons as isolated. We have five electrons occupying the six $3d_\epsilon$ states and can treat this as a "hole" in a completed subshell, greatly simplifying the calculation.

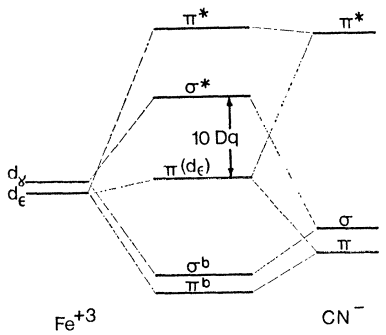

FIG. 12. A diagram showing the molecular energy levels in $K_3Fe(CN)_6$. The ground state has five electrons in the six states available in the $\pi(d_\epsilon)$ level. The degeneracy of these states is removed by a rhombic crystal field.

Relative to cubic axes which join the CN ligands to the Fe, we define the $3d_\epsilon$ basis states as follows:

$$\begin{aligned} |x'y'\rangle &= i/\sqrt{2}(Y_2'^2 - Y_1'^{-2}), \\ |x'z'\rangle &= -1/\sqrt{2}(Y_2'^1 - Y_2'^{-1}), \\ |y'z'\rangle &= i/\sqrt{2}(Y_2'^1 + Y_2'^{-1}), \end{aligned} \tag{1}$$

where x', y', z' are the cubic axes of the molecule. Suppose now that the system experiences a distortion of low symmetry, which we represent as a crystal-field potential $V = A\bar{z}^2/r^2 + B\bar{x}^2/r^2 + C\bar{y}^2/r^2$, where $C = -(A+B)$ and $\bar{x}, \bar{y}, \bar{z}$ are the principal axes of V. If the primed and barred systems are identical, then the wave functions of (1) are energy eigenfunctions in the orthorhombic crystal field. In the more general case of triclinic symmetry, we have energy eigenfunctions given by

$$\begin{aligned} |a\rangle &= l_{zz}|x'y'\rangle + l_{zy}|x'z'\rangle + l_{zx}|y'z'\rangle, \\ |b\rangle &= l_{xz}|x'y'\rangle + l_{xy}|x'z'\rangle + l_{xx}|y'z'\rangle, \\ |c\rangle &= l_{yz}|x'y'\rangle + l_{yy}|x'z'\rangle + l_{yx}|y'z'\rangle. \end{aligned} \tag{2}$$

Since these eigenstates are orthonormal, the coefficients l_{ij} behave like the set of direction cosines relating one set of Cartesian axes to another. With commendable foresight, we choose to calculate the g tensor in the x, y, z system which is related to the cubic (primed) axes by $x_i = l_{ij}x_j'$. The expressions (2) represent a rotation in *function* space. It will be convenient to express the angular momentum operators in the unprimed system. Since $\mathbf{L}$ is a vector we have $L_i = l_{ij}L_j'$. Following Bleaney,[8] the nonzero matrix elements of $\mathbf{L}'$ are $\langle x'y'|L_y'|y'z'\rangle = -\langle y'z'|L_y'|x'y'\rangle = ik$ and permutations where the orbital reduction factor k allows for possible covalency effects. We then have

$$\begin{aligned} \langle a|L_i|b\rangle &= -\langle b|L_i|a\rangle = ikl_{ij}l_{yj} = ik\delta_{iy}, \\ \langle b|L_i|c\rangle &= -\langle c|L_i|b\rangle = ikl_{ij}l_{zj} = ik\delta_{iz}, \\ \langle c|L_i|a\rangle &= -\langle a|L_i|c\rangle = ikl_{ij}l_{xj} = ik\delta_{ix}. \end{aligned} \tag{3}$$

[18] R. G. Shulman and S. Sugano, J. Chem. Phys. 42, 39 (1965).
[19] J. Howard, J. Chem. Phys. 3, 813 (1935).

We now introduce the spin variable and consider the effect of the spin-orbit interaction $\lambda\mathbf{L}\cdot\mathbf{S}$ in the basis states defined below. The interaction matrix $\mathcal{H}'=V+\lambda\mathbf{L}\cdot\mathbf{S}$ is[20]

$\|a\rangle\alpha$	$\|b\rangle\beta$	$i\|c\rangle\beta$	$\|a\rangle\beta$	$\|b\rangle\alpha$	$i\|c\rangle\alpha$
$-2A/7$	$\lambda/2$	$\lambda/2$	0	0	0
$\lambda/2$	$-2B/7$	$\lambda/2$	0	0	0
$\lambda/2$	$\lambda/2$	$-2C/7$	0	0	0
0	0	0	$-2A/7$	$-\lambda/2$	$\lambda/2$
0	0	0	$-\lambda/2$	$-2B/7$	$-\lambda/2$
0	0	0	$\lambda/2$	$-\lambda/2$	$-2C/7$

Diagonalization of the two 3×3 irreducible matrices yields three 2-fold degenerate eigenstates of the form

$$\begin{aligned}|+_n\rangle&=a_n|a\rangle\alpha+b_n|b\rangle\beta+ic_n|c\rangle\beta,\\ |-_n\rangle&=a_n|a\rangle\beta-b_n|b\rangle\alpha+ic_n|c\rangle\alpha,\end{aligned}\tag{4}$$

having energy E_n, where $n=1$, 2, 3 and the a_n, b_n, c_n can be taken as real because the matrix elements are all real. The degeneracy is of course required by Kramers's theorem.

Using these eigenstates, we can calculate the g values and the susceptibility as functions of a_n, b_n, c_n. Consider an applied magnetic field $\mathbf{H}$, which induces a magnetic moment in the paramagnetic salt, not necessarily in the direction of $\mathbf{H}$. We define the magnetic moment operator $\mathbf{P}=\mathbf{L}+2\mathbf{S}=\tilde{g}\cdot\mathbf{S}_{\text{eff}}$ (or $P_i=g_{ij}S_{\text{eff}j}$), where $\mathbf{S}_{\text{eff}}$ is the effective spin operator for the Kramers doublet (i.e., $S_{\text{eff}z}|+\rangle=+\frac{1}{2}|+\rangle$ and $S_{\text{eff}z}|-\rangle=-\frac{1}{2}|-\rangle$). We can then calculate the matrix elements of the g tensor with the aid of Eqs. (3) and the formulas derived in the Appendix, assuming only that the electronic ground state is occupied:

$$\begin{aligned}&g_{xx}=2(a_1^2-b_1^2+c_1^2+2ka_1c_1),\quad g_{xy}=g_{xz}=g_{yz}=0\\ &g_{yy}=2(a_1^2+b_1^2-c_1^2+2ka_1b_1),\\ &g_{zz}=2(a_1^2-b_1^2-c_1^2-2kb_1c_1).\end{aligned}$$

This indicates that the principal axes of $\tilde{g}$ coincide with x, y, z. Bleaney and O'Brien[8] successfully fitted the experimentally measured g values[7] of $g_{xx}=0.91$, $g_{yy}=2.35$, $g_{zz}=2.10$ by using $a_1=0.524$, $b_1=0.702$, $c_1=0.482$ and an orbital reduction factor of $k=0.875$. The orbital reduction factor reflects the fact that the hole travels over the entire complex and is not confined to the Fe site alone. Ballhausen[21] derives a formula for $k=1-\frac{1}{2}N^2A_\pi^2$, where $\psi=N(\psi_{\text{Fe}}+A_\pi\psi_{1ig})$. Neglecting overlap, this leads to a value of $N^2\sim0.75$.

The parameters A/λ and B/λ are determined from the experimental g values. These in turn determine a_n, b_n, c_n, and E_n/λ for $n=1$, 2, 3. The susceptibilities can then be calculated, and a comparison with the observed temperature dependence yields λ. Bleaney found $\lambda=-278$ cm^{-1} for $K_3Fe(CN)_6$, indicating the following values for the Kramers doublets:

$$\begin{aligned}&E_1=-288.98\text{ cm}^{-1}, && a_1=+0.524,\\ &E_2=+102.26, && a_2=+0.605,\\ &E_3=+186.72, && a_3=+0.599,\\ &b_1=+0.702, && c_1=+0.482,\\ &b_2=-0.705, && c_2=+0.369,\\ &b_3=+0.098, && c_3=-0.795.\end{aligned}\tag{5}$$

The corresponding crystal-field energies (which would be eigenenergies in the absence of spin-orbit coupling) are $E_{xy}=25.19$ cm^{-1}, $E_{yz}=-98.9$ cm^{-1}, and $E_{xz}=64.7$ cm^{-1}. The Kramers doublets found here will be used in the calculations of the hyperfine interactions, keeping in mind that the basis states are really molecular orbitals.

It was found experimentally[7] that the g-tensor axes of $K_3Fe(CN)_6$ are rotated about the cubic z' axes by an angle $\gamma=45°$. We have found above that in the electronic interaction with an external magnetic field the relative orientation of the cubic system and the g tensor does not enter. We will find below that the same is not true of the hyperfine interactions.

B. Quadrupole Interaction

In its 14.4-keV excited state, the Fe^{57} nucleus has a slightly elongated charge distribution, which can interact with the quadratic components of the local electrostatic potential. This electric quadrupole interaction provides a probe for the study of the electronic charge which is the source of the potential. In its principal axis systems, the quadrupole interaction Hamiltonian is given by

$$\mathcal{H}_Q=\frac{eQ}{4I(2I-1)}\{V_{\bar{z}\bar{z}}[3I_{\bar{z}}^2-I(I+1)]+(V_{\bar{x}\bar{x}}-V_{\bar{y}\bar{y}})(I_{\bar{x}}^2-I_{\bar{y}}^2)\}.\tag{6}$$

The quadratic potential or electrostatic field gradient (EFG) arises from two sources.[6]

(1) The nonspherical distribution of the valence electrons on the Fe ion. These are electrons external to closed shells and non-S in symmetry. (It is worth noting that the filled molecular orbitals will have cubic symmetry and will not contribute to the EFG.) This contribution to the EFG can be temperature-dependent via excitations to low-lying empty orbitals.

(2) The EFG created by the noncubic charge distribution about the iron site in the lattice. This may be temperature-dependent especially if the lattice expansion with temperature is not isotropic.

Both effects (1) and (2) are modified by distortions of the ion core. These reduce the EFG of the valence

[20] We have chosen our states as $|a\rangle$, $|b\rangle$, and $i|c\rangle$ so that the Hamiltonian matrix above is *real*.

[21] C. J. Ballhausen, *Introduction to Ligand Field Theory* (McGraw-Hill Book Co., New York, 1962), p. 154.

electrons and enhance that of the more distant charges. The relevant correction factors are the Sternheimer shielding factors.[22] In the principal axis system of the EFG, the matrix elements of $\mathcal{H}_Q$ between the different I_z levels of the Fe^{57} first excited state ($I=\frac{3}{2}$) are

$$\mathcal{H}_Q=\tfrac{1}{2}eQ\begin{array}{c|cccc} & |+\frac{3}{2}\rangle & & |+\frac{1}{2}\rangle & \\ \langle+\frac{3}{2}| & \frac{1}{2}V_{zz} & & 0 & \\ & 0 & & -\frac{1}{2}V_{zz} & \\ \langle+\frac{1}{2}| & \frac{1}{2}(V_{xx}-V_{yy})/\sqrt{3} & & 0 & \\ & 0 & & \frac{1}{2}(V_{xx}-V_{yy})/\sqrt{3} & \end{array}$$

$$\begin{array}{c|cccc} & |-\frac{1}{2}\rangle & & |-\frac{3}{2}\rangle & \\ \langle-\frac{1}{2}| & \frac{1}{2}(V_{xx}-V_{yy})/\sqrt{3} & & 0 & \\ & 0 & & \frac{1}{2}(V_{xx}-V_{yy})/\sqrt{3} & \\ \langle-\frac{3}{2}| & -\frac{1}{2}V_{zz} & & 0 & \\ & 0 & & \frac{1}{2}V_{zz} & \end{array}.$$

In the nuclear ground state, $Q=0$. Diagonalization yields two 2-fold degenerate eigenstates, with the degeneracy again a result of Kramers's theorem. The difference in energy between these two levels is

$$\Delta E=\tfrac{1}{2}e^2Qq(1+\eta^3/3)^{1/2},$$

where $eq=V_{zz}$ and $\eta=(V_{xx}-V_{yy})/V_{zz}$ is the asymmetry parameter which arises when the axial symmetry of the EFG is lost. Next we must evaluate

$$\begin{aligned} q&=V_{zz}/e=(1-R)q_{\rm val}+(1-\gamma_\infty)q_{\rm lat},\\ \eta q&=(V_{xx}-V_{yy})/e=(1-R)\eta q_{\rm val}+(1-\gamma_\infty)\eta q_{\rm lat}, \end{aligned} \tag{7}$$

where $(1-R)$ and $(1-\gamma_\infty)$ are the Sternheimer factors. $q_{\rm val}$ and $\eta q_{\rm val}$ are the contributions to the EFG from the valence electrons. The following are derived in the Appendix:

$$\begin{aligned} q_{\rm val}&=N^2\langle r^{-3}\rangle\left(\frac{16\pi}{5}\right)^{1/2}\frac{\sum_i\langle i|\,Y_2^0\,|i\rangle e^{-E_i/kT}}{\sum_i\langle i|i\rangle e^{-E_i/kT}}\\ &=N^2\langle r^{-3}\rangle\frac{\sum_i\{-(4/7)a_i^2+(2/7)(b_i^2+c_i^2)\}e^{-E_i/kT}}{\sum_i e^{-E_i/kT}}\\ \eta q_{\rm val}&=N^2\langle r^{-3}\rangle\left(\frac{24\pi}{5}\right)^{1/2}\frac{\sum_i\langle i|\,Y_2^2+Y_2^{-2}\,|i\rangle e^{-E_i/kT}}{\sum_i\langle i|i\rangle e^{-E_i/kT}}\\ &=N^2\langle r^{-3}\rangle\frac{\sum_i(6/7)(c_i^2-b_i^2)e^{-E_i/kT}}{\sum_i e^{-E_i/kT}}, \end{aligned} \tag{8}$$

where $|i\rangle$ and E_i are the electronic wave functions and energies as found in (5) and N^2 is the covalency factor. Note that the sign of the EFG corresponds to a positive "hole". The expressions above are correct in the principal axis system of the EFG and are thermal averages over the three doublets. The question of relative orientation of the various axis systems will be deferred to a subsequent section.

The contributions of the noncubic charge distribution in the lattice to the EFG may be estimated in several ways. However, in the case of $K_3Fe(CN)_6$ we are fortunate to have an isomorphic salt $K_3Co(CN)_6$ whose valence electrons have cubic symmetry because of a "closed shell" configuration $(3d_\epsilon)^6$ so that $q_{\rm val}=0$. NMR measurements of the quadrupole splitting in $K_3Co(CN)_6$ have been made[23] and by knowing $Q_{Co^{59}}$ one can determine $(1-\gamma_\infty)q_{\rm lat}$. Because of the cubic symmetry of the filled $3d_\epsilon$ shell, we assume that the EFG in $K_3Co(CN)_6$ is due purely to the lattice and that the same EFG is produced by the lattice in $K_3Fe(CN)_6$. This is probably a fair assumption, since the two crystals have identical lattice parameters.[9]

C. Magnetic Hyperfine Interaction

Both the excited and ground states of Fe^{57} interact with the magnetic fields. We consider now their interaction with the internal magnetic fields which arise in the presence of unpaired electron spin. The relevant Hamiltonian is

$$\begin{aligned} \mathcal{H}_M&=P\sum_k[\mathbf{I}\cdot\mathbf{l}_k+3(\mathbf{I}\cdot\hat{r}_k)(\mathbf{s}_k\cdot\hat{r}_k)-\mathbf{I}\cdot\mathbf{s}_k-\kappa\mathbf{I}\cdot\mathbf{s}_k]\\ &=\mathbf{I}\cdot\bar{A}\cdot\mathbf{S}_{\rm eff}\\ &=A_xI_xS_x+A_yI_yS_y+A_zI_zS_z+C_{xy}(S_xI_y-S_yI_x), \end{aligned} \tag{9}$$

where $P=2g_n\beta_n\beta_e\langle r^{-3}\rangle N^2$. $\mathcal{H}_M$ is made up of the following contributions:

(1) the interaction between the nuclear magnetic moment and the current loops caused by the orbital motion of the electrons (first term),

(2) the dipolar interaction between the magnetic moment of the nucleus and the magnetic moments of the unpaired electrons (second and third terms), and

(3) the Fermi contact interaction between the nuclear magnetic moment and the polarized S electrons which exist at the nucleus (last term). The paired S electrons experience spin-dependent exchange forces with the unpaired 3d electrons. We then have $|\psi_S{}^\uparrow(0)|^2\neq|\psi_S{}^\downarrow(0)|^2$, a spin density at the nucleus which is proportional to the amount of unpaired 3d spin.

Because the magnetic hyperfine interaction in $K_3Fe(CN)_6$ is observable only at low temperatures we will be concerned only with the matrix elements of H_M between members of the ground doublet. It is convenient to calculate these in the principal axis system of the g tensor. We present here the expressions for the components of the magnetic hyperfine interaction tensor $\bar{A}$, and refer the reader to the Appendix for the

[22] R. M. Sternheimer, Phys. Rev. **130**, 1423 (1963); G. Burns, *ibid.* **124**, 524 (1961).

[23] T. Sugawara, J. Phys. Soc. Japan **24**, 858 (1959).

TABLE I. Hamiltonian matrix $\mathcal{H}=\beta_e\mathbf{H}\cdot\tilde{g}\cdot\mathbf{S}_{\rm eff}+\mathbf{I}\cdot\tilde{A}\cdot\mathbf{S}_{\rm eff}+\mathcal{H}_Q+\beta_n g_n\mathbf{H}\cdot\mathbf{I}$ for Fe^{57} excited state.

$p=1$	2	3	4	5	6	7	8
$\lvert+,+\frac{3}{2}\rangle$	$\lvert+,+\frac{1}{2}\rangle$	$\lvert+,-\frac{1}{2}\rangle$	$\lvert+,-\frac{3}{2}\rangle$	$\lvert-,+\frac{3}{2}\rangle$	$\lvert-,+\frac{1}{2}\rangle$	$\lvert-,-\frac{1}{2}\rangle$	$\lvert-,-\frac{3}{2}\rangle$
$\frac{3}{4}A_z+\frac{1}{2}\beta_e g_z H_z$	$(\sqrt{\frac{3}{4}})\beta_n g_n(H_z-iH_y)$	$\frac{1}{4}e^2Qq/\sqrt{3}$	0	$\frac{1}{2}\beta_e(g_xH_x-ig_yH_y)$	$\frac{1}{4}\sqrt{3}(A_x-A_y)$	0	0
$+\frac{1}{2}\beta_n g_n H_z+\frac{1}{4}e^2Qq$	$\frac{1}{4}A_z+\frac{1}{2}\beta_e g_z H_z$	$g_n\beta_n(H_x-iH_y)$	$\frac{1}{4}e^2Qq/\sqrt{3}$	$\frac{1}{4}\sqrt{3}(A_x+A_y+2iC_{xy})$	$\frac{1}{2}\beta_e(g_xH_x-ig_yH_y)$	$\frac{1}{2}(A_x-A_y)$	0
	$+\frac{1}{2}\beta_n g_n H_z-\frac{1}{4}e^2Qq$	$(\sqrt{\frac{3}{4}})\beta_n g_n(H_x-iH_y)$	0	$\frac{1}{2}(A_x+A_y+2iC_{xy})$	$\frac{1}{2}\beta_e(g_xH_x-ig_yH_y)$	$\frac{1}{4}\sqrt{3}(A_x+A_y+2iC_{xy})$	$\frac{1}{4}\sqrt{3}(A_x-A_y)$
		$-\frac{1}{2}\beta_n g_n H_z-\frac{1}{4}e^2Qq$	$-\frac{3}{4}A_z+\frac{1}{2}\beta_e g_z H_z$	0	$(\sqrt{\frac{3}{4}})\beta_n g_n(H_x-iH_y)$	$\frac{1}{4}e^2Qq/\sqrt{3}$	0
			$-\frac{3}{2}\beta_n g_n H_z+\frac{1}{4}e^2Qq$	$-\frac{1}{4}A_z-\frac{1}{2}\beta_e g_z H_z$	$\beta_n g_n(H_z-iH_y)$	$\frac{1}{4}e^2Qq/\sqrt{3}$	$(\sqrt{\frac{3}{4}})\beta_n g_n(H_x-H_y)$
				$+\frac{3}{2}\beta_n g_n H_z+\frac{1}{4}e^2Qq$	$\frac{1}{4}A_z-\frac{1}{2}\beta_e g_z H_z$	$(\sqrt{\frac{3}{4}})\beta_n g_n(H_x-H_y)$	$\frac{3}{4}A_z-\frac{1}{2}\beta_e g_z H_z$
					$-\frac{1}{2}\beta_n g_n H_z-\frac{1}{4}e^2Qq$	$\frac{3}{4}A_z-\frac{1}{2}\beta_e g_z H_z$	$-\frac{3}{2}\beta_n g_n H_z+\frac{1}{4}e^2Qq$

(complex conjugate)

derivations:[24]

$$
\begin{aligned}
A_z&=P[-4bc-(1+\kappa)(a^2-b^2-c^2)\\
&\quad+3(a^2-3b^2-3c^2)/7+6a(b+c)/7],\\
(A_x+A_y+2iC_{xy})&\\
&=P\{+4a(b+c)-2(1+\kappa)a^2+18a^2/7\\
&\quad-6[a(b+c)-(b-c)^2e^{+4i\gamma}]/7\},\\
(A_x-A_y)&=P[+4a(c-b)-(1+\kappa)(c^2-b^2)2\\
&\quad+12(c^2-b^2)/7+6a(c-b)/7].
\end{aligned}
\tag{10}
$$

γ is a rotation about z which relates the g system to the cubic system (Fig. 1). The presence of a complex term in $\tilde{A}$ indicates that for arbitrary γ the principal axes of $\tilde{A}$ do not coincide with those of $\tilde{g}$.

In the expression for P, $\langle r^{-3}\rangle$ refers to the expectation value for an electron in a 3d orbital of the Fe ion. We will use the value $5.72/a_0^3$ found by Freeman and Watson.[25] The factor N^2 accounts for the probability of finding the electron in this orbital on the Fe ion. Because they involve small values of r^{-3}, contributions from the overlap regions and from the CN are negligible. We are thus using a covalency factor N^2 for the magnetic and electric hyperfine interactions which is smaller than k, the orbital reduction factor of the g calculation. The reason is that the r^{-3} factor is not present in the latter, and contributions from the remote parts of the wave function are significant. We will adjust N^2 to fit the experiment and then compare it with some theoretical estimates.

The Fermi contact factor is related to the spin polarization produced by unpaired 3d electrons by

$$
\begin{aligned}
N^2\langle r^{-3}\rangle\kappa&=-(8\pi/3)N^2(|\psi_S{}^{\uparrow}(0)|^2-|\psi_S{}^{\downarrow}(0)|^2)\\
&=-\tfrac{2}{3}\chi N^2.
\end{aligned}
\tag{11}
$$

The calculation of Freeman and Watson[25] yields $\chi=-3.0/a_0^3$ for a single unpaired spin in the 3d shell. Hence $\kappa=+0.35$, a result which has been found to fit the hyperfine spectra of hemoglobin cyanide.[26] It is known that the effective field at the nucleus decreases with increasing covalency,[27] and we assume that the contact interaction is scaled by the factor N^2 as our previous expressions imply.

D. Total Hamiltonian; Relative Orientations of $\tilde{A}$ and EFG

Both high temperature and high paramagnetic concentration cause the magnetic hyperfine interaction to be washed out by rapid spin relaxation. In such cases

[24] a, b, and c are really a_1, b_1, and c_1 since only the ground state is occupied at the low temperatures required to observe these effects. In the interest of simplicity we have dropped the subscript here. $C_{xy}\neq 0$ because of monoclinic symmetry.

[25] R. E. Watson and A. J. Freeman, Phys. Rev. **123**, 2027 (1961); in *Magnetism*, edited by G. Rado and H. Suhl, (Academic Press Inc., New York, 1965), Vol. 11A, p. 291.

[26] G. Lang and W. Marshall, Proc. Phys. Soc. (London) **87**, 3 (1966).

[27] J. C. M. Henning, Phys. Letters **24A**, 40 (1967). J. S. Van Wieringgen, Discussions Faraday Soc. **119**, 118 (1955).

TABLE II. Ground-state Fe^{57} Hamiltonian.

$q=1$	2	3	4
$\lvert+,+\frac{1}{2}\rangle$	$\lvert+,-\frac{1}{2}\rangle$	$\lvert-,+\frac{1}{2}\rangle$	$\lvert-,-\frac{1}{2}\rangle$
$\{\frac{1}{4}A_z+\frac{1}{2}g_z\beta_e H_z+\frac{1}{2}g_n\beta_n H_z\}$	$\frac{1}{2}g_n\beta_n(H_x-iH_y)$	$\frac{1}{2}\beta_e(g_xH_x-ig_yH_y)$	$\frac{1}{4}(A_x-A_y)$
	$\{-\frac{1}{4}A_z+\frac{1}{2}\beta_e g_z H_z-\frac{1}{2}\beta_n g_n H_z\}$	$\frac{1}{4}(A_x+A_y+2iC_{xy})$	$\frac{1}{2}\beta_e(g_xH_x-ig_yH_y)$
		$\{-\frac{1}{4}A_z-\frac{1}{2}\beta_e g_z H_z+\frac{1}{2}\beta_n g_n H_z\}$	$\frac{1}{2}\beta_n g_n(H_x-iH_y)$
	(complex conjugate)		$\{\frac{1}{4}A_z-\frac{1}{2}\beta_e g_z H_z-\frac{1}{2}\beta_n g_n H_z\}$

only a quadrupole interaction is present and the Hamiltonian $\mathcal{H}_Q$ applies. Since it does not operate on electronic states, the eigenvalue problem may be treated using basis states which are just the nuclear spin states, with the electronic state determining the EFG. When magnetic hyperfine interaction is present the problem becomes more complicated because the Hamiltonian operator has matrix elements between the two members of the Kramers doublet. The basis states must then be taken as products of nuclear and electronic wave functions, and we must find the eigenstates of the combined system. At low temperatures, states involving only the electronic ground doublet will enter. The inclination of two of the g-tensor axes relative to the cubic axes introduces further complications, which we now attempt to clarify.

Consider the Fe ion acted upon by a cubic crystal field plus a potential V (the rhombic field) quadratic in the coordinates, whose principal axes align with the cubic axes. The crystal-field eigenstates are $|y'z'\rangle$, $|z'x'\rangle$, and $|x'y'\rangle$. Spin-orbit coupling mixes them, but the rhombic symmetry is preserved, i.e., the cubic axes are principal axes of $\tilde{g}$, $\tilde{A}$, and the EFG. Imagine now that the V field is rotated by an angle γ about z as an axis, the cubic field (x', y', and z') remaining fixed, giving monoclinic symmetry. The calculations of the Appendix show that the EFG follows $V(\bar{x},\bar{y},\bar{z})$ and maintains constant magnitude. The principal axes of the $\tilde{g}$ tensor (x,y,z) on the other hand, rotate through an angle $-\gamma$ about z. the $\tilde{A}$ tensor also rotates about z, but through an angle which depends on the relative strength of the rhombic field and the spin-orbit coupling constant. The d_ϵ states do not rotate as a whole. In this particular case the contours of $|b\rangle$ and $|c\rangle$ rotate with V, while $|a\rangle$ remains as $|x'y'\rangle$, i.e., aligned in the cubic system. In a more general rotation of V, the behavior of the d_ϵ states would not be simple.

We have already calculated $\tilde{g}$ and $\tilde{A}$ in the principal axis system of $\tilde{g}$. It is shown in the Appendix that the quadrupole interaction is expressed correctly in the $\tilde{g}$ system if we multiply ηq in (8) by $e^{+4i\gamma}$. According to Baker *et al.*[7] the angle γ for $K_3Fe(CN)_6$ is 45°, so that the net effect is merely a change in the sign of η. In order to make specific the results of this section we now display the complete Hamiltonian matrix in the x, y, z system, including the interaction with an external applied field $\mathbf{H}$. Corresponding to the nuclear excited state, we have the matrix in Table I. The basis states are indicated in the first row. The symbols $|+\rangle$ and $|-\rangle$ refer to the two members of the electronic ground doublet (5), and the states are written as $|\pm, I_z\rangle$. For the nuclear ground state, we have the matrix in Table II. p and q are labels given to the components of each eigenstate.

For convenience we tabulate the values which will be assumed for the various parameters unless specifically stated otherwise: $Q=0.18$ b,[28] $q_{\text{lat}}=-0.065\times10^{+24}$ cm^{-3}, $\eta_{\text{lat}}=0.75$ [23], $(1-R)=0.68$, $(1-\gamma_\infty)=10.0$,[29] $P=2\beta_e\beta_n g_n\langle r^{-3}\rangle N^2=-4.8N^2$ (mm/sec) for the nuclear excited state where $\langle r^{-3}\rangle N^2=4.00\pm0.10/a_0^3$, $g_n=-0.102$ for excited state of Fe^{57}, $g_n=+0.1806$ for ground state of Fe^{57}, A_x, A_y, A_z, and C_{xy} as given in Eq. (10), q and ηq are given in Eqs. (8), $e^2Q/4=0.135\times10^{-24}$ mm/sec cm^3 for $Q=0.18$ b, $\gamma=45°$, $\kappa=+0.35\pm0.02$, $\beta_n=\beta_e/1836$, $\beta_e=0.928\times10^{-20}$ erg/G$=0.121$ mm/sec/G.

E. Case of an Applied Field, Including Fast Relaxation

The magnetic Hamiltonian (9) requires us to treat the nucleus and electrons at the same time, using wave functions which have nuclear and electronic parts. Because the nucleus produces fields of the order of 10 G at the electrons it is possible to decouple the particles by applying fields of a few hundred gauss. Under these conditions the behavior of the electron is dominated by its interaction with the external magnetic field and two electronic states which are solutions of the Hamiltonian $\mathcal{H}_e=\beta_e\mathbf{H}\cdot\tilde{g}\cdot\mathbf{S}_{\text{eff}}$ with energies $E_\uparrow$ and $E_\downarrow$. Here we have considered the ground-state Kramers doublet only. The Mössbauer spectrum is then the sum of two contributions, each determined by Hamiltonians of the form

$$\mathcal{H}=\mathbf{I}\cdot[\tilde{A}\cdot\langle\mathbf{S}_{\text{eff}}\rangle+g_n\beta_n\mathbf{H}]+\mathcal{H}_Q, \qquad (12)$$

where $\langle S_{\text{eff}}\rangle$ has opposite direction for the two members of the doublet. The Mössbauer spectra are added with weights $e^{-E\uparrow/kT}$ and $e^{-E\downarrow/kT}$, respectively. The first term in the bracket corresponds to several hundred kilogauss so that the second is usually negligible.

[28] C. E. Johnson, Proc. Phys. Soc. (London) **92**, 748 (1967).

[29] We can estimate the Sternheimer factors for low-spin ferric ions by comparing with high-spin ferrous ions since in each case we are dealing with a hole or electron external to a spherically symmetric shell of charge [B. A. Scott and R. A. Bernheim, J. Chem. Phys. **44**, 2004 (1965); Phys. Rev. **123**, 2070 (1961)]. $(1-\gamma_\infty)$ is estimated to be about 8.0 in $K_3Co(CN)_6$ and about 10.0 in $K_3Fe(CN)_6$.

Because the spectrum doesn't depend upon the sign of the vector in the bracket, it shows little field dependence once decoupling is achieved. For intermediate fields (where there is still some coupling between electron and nucleus) one must use the full Hamiltonian

$$\mathcal{H}=\beta_e\mathbf{H}\cdot\tilde{g}\cdot\mathbf{S}_{\text{eff}}+\mathbf{I}\cdot\tilde{A}\cdot\mathbf{S}_{\text{eff}}+\mathcal{H}_Q+g_n\beta_n\mathbf{H}\cdot\mathbf{I}. \quad (13)$$

If the electron spin undergoes fast relaxation (as in concentrated material) the situation is considerably different. Here the electron undergoes transitions between its two possible states at a rate which exceeds the Larmor frequency of the nucleus. The nucleus is unable to follow the rapid fluctuations of the field and senses only the thermal average spin. The Hamiltonian is of the form

$$\mathcal{H}=\mathbf{I}\cdot[\tilde{A}\cdot\langle\mathbf{S}_{\text{eff}}\rangle_T+g_n\beta_n\mathbf{H}]+\mathcal{H}_Q, \quad (14)$$

where

$$\langle\mathbf{S}_{\text{eff}}\rangle_T=\sum_i\langle i|\mathbf{S}_{\text{eff}}|i\rangle e^{-E_i/kT}/\sum_i\langle i|i\rangle e^{-E_i/kT}.$$

Through $\langle\mathbf{S}_{\text{eff}}\rangle_T$ the strength of the nuclear magnetic interaction and hence the shape of the Mössbauer spectrum depends strongly upon the strength of the applied field and the temperature.

F. Transition Probabilities—Calculation of Mössbauer Spectrum

The first step in finding the Mössbauer absorption spectrum is the determination of the eigenstates and energies which result from the Hamiltonians above. For any particular case with the matrices in numerical form the solutions are easily found using digital computing techniques. The energy of one of the possible Mössbauer transitions (E_{kl}) is found by subtracting the ground-state energy E_l from the excited state energy E_k. The second step is to determine the γ-absorption transition probabilities between each ground state and all possible excited states. The transition amplitudes are the matrix elements of the magnetic dipole interaction between γ ray and nucleus. The electronic coordinates do not enter this operator, so the amplitude is proportional to the projection of the electronic part of the ground state in question onto the electronic part of the excited state. Less formally, the electron does not change its state in the Mössbauer transition.

We now consider the transition probabilities associated with an unpolarized γ beam traveling in the direction θ, ϕ relative to the unprimed (g tensor) axis system (Fig. 1). The probability amplitude for a transition between energy eigenstates k and l is

$$\text{Amp}_{kl}=\sum_{p=1}^{4}\sum_{q=1}^{2}F_{kp}G_{lq}{}^{*}C(\tfrac{1}{2}1\tfrac{3}{2};I_{zq}mI_{zp})\mathbf{X}_1{}^m(\theta,\phi)$$
$$+\sum_{p=5}^{8}\sum_{q=3}^{4}F_{kp}G_{lq}{}^{*}C(\tfrac{1}{2}1\tfrac{3}{2};I_{zq}mI_{zp})\mathbf{X}_1{}^m(\theta,\phi), \quad (15)$$

where F_{kp} is the pth component of the kth nuclear excited state and G_{lq} is the qth component of the lth nuclear ground state. The $C(\frac{1}{2}1\frac{3}{2};I_{zq}mI_{zp})$ are the well-known Clebsch-Gordan coefficients where $m=I_{zp}-I_{zq}$ and the $\mathbf{X}_1{}^m(\theta,\phi)$ are the vector spherical harmonics.[30] We will discuss the transition probabilities in the presence of an applied magnetic field. The zero-field situation is then taken into account by setting H_{ext} equal to zero. In the single-crystal experiments the directions of γ-ray incidence and applied field are known. The Mössbauer absorption probabilities are found by taking the absolute squares of the amplitudes (15). The total spectrum is the sum of contributions from the two differently oriented sites. For polycrystalline specimens only fields perpendicular or parallel to the γ beam will be considered. In each case a numerical averaging procedure is necessary. In the parallel case we have found the net spectrum by summing over 100 different field directions distributed uniformly over an octant of the unit sphere. The case of transverse applied field is similar except for an additional average taken over two directions of γ incidence which are perpendicular to each other and to H_{ext}. Ideally, the finite energy width of the nuclear excited state would be taken into account by folding all these calculated spectra into a Lorentzian of appropriate width. Instrumental defects and relaxation processes often broaden the line further, and a linewidth which is greater than natural is then appropriate.

5. DISCUSSION

We compare the known experimental facts with two electronic models labelled I and II. Model I is the orthorhombic crystal field + spin orbit as proposed by Bleaney and O'Brien for the dilute salt[8] and given by Eq. (5). Model II is a modification of model I in that the crystal-field parameters A and C are interchanged. In the ground state of model I, the magnetic electron is found with probabilities $a^2=0.27$ in the state $|a\rangle$ and $c^2=0.23$ in the state $|c\rangle$. It requires only a relatively small change in the crystal field to reverse this electron distribution and thus to change model I into model II.

Model II corresponds to the $g=2.09$ and $g=2.34$ directions interchanged from those reported for the dilute salt.[7] The interchange appears to occur in the concentrated salt, although the ESR results are ambiguous.

The magnetic susceptibility data[8] indicate that at low temperature the largest magnetic moment in the concentrated salt is near the b axis in the crystal as indicated by model II. However, as the temperature is raised or the concentration of Fe is lowered, the magnitude of the moment near the a axis overtakes that near the b axis. This crossover in the susceptibilities occurs at about 70°K.

In our treatment of the quadrupole split spectra of $K_3Fe(CN)_6$, the parameter values obtained from the

[30] S. De Benedetti, *Nuclear Interactions* (J. Wiley & Sons, Inc., New York, 1964), p. 264.

TABLE III. Single-crystal area ratios.[a]

Direction of γ's relative to the crystal axes	R_{exp} (20°K)	(70°K)	R_{calc}(0°K) Model I (II)	Best fit to experiment	R_{exp} (300°K)	R_{calc}(300°K) Model I (II)	Best fit to experiment
(1) Parallel to a' axis	1.69	1.73	1.64(1.61)	1.74	2.10	1.72(1.78)	2.10
(2) 27° from a' axis in a'-b plane	1.32	1.35	1.50(1.42)	1.45	1.48	1.53(1.46)	1.58
(3) 45° from a' axis in a'-b plane	1.15	1.17	1.33(1.21)	1.15	1.28	1.47(1.21)	1.21
(4) 63° from a' axis in a'-b plane	0.94	0.95	1.18(1.03)	0.88	0.95	1.22(0.99)	0.89
(5) Parallel to the b axis	0.77	0.76	1.10(0.93)	0.74	0.72	1.12(0.86)	0.72
(6) 117° from a' axis in a'-b plane	0.84	0.84	1.18(1.03)	0.88	0.84	1.22(0.99)	0.89
(7) 45° from c axis in b-c plane	0.74	0.71	0.80(0.80)	0.74	0.66	0.78(0.77)	0.70
(8) Parallel to c axis	0.79	0.76	0.60(0.69)	0.78	0.69	0.51(0.60)	0.68
(9) 45° from c axis a'-c plane	1.13	1.12	1.02(1.05)	1.14	1.13	0.95(1.07)	1.17

[a] The angle between the z and b axes is δ in Fig. 1. For 300°K, $\delta=25°$; for 0–77°K, $\delta=30°$.

magnetically split spectra of the dilute material are used. We make the somewhat illogical choice of discussing the quadrupole spectra first, however, because these are more generally understood and are the main concern of many workers in the field.

A. Quadrupole Interaction

The dominant contribution to the quadrupole splitting in $K_3Fe(CN)_6$ results from the electrostatic field gradient which is produced by the asymmetry in the iron d-electron distribution. The g values provide us with a knowledge of this asymmetry in the three lowest-lying Kramers doublets (i.e., with the values a_1, b_1, c_1), and the temperature dependence of the susceptibility yields their energy separation. The quantity $N^2\langle r^{-3}\rangle_{3d}$ is found to be $4.0\pm0.1/a_0^3$ from the magnetically split Mössbauer spectra (see below). With this information we can evaluate the EFG expressions (8). Only the valence electron shielding parameter $(1-R)$ is then required to determine the net valence electron contribution to the EFG at the nucleus. Using Ingall's value of 0.68 for $(1-R)$ we find the values shown in column 1 of Table IV. Using the value of 0.18 b for the nuclear quadrupole moment[6,28] and considering valence electron contributions only, we calculate the quadrupole splitting shown as a function of temperature in curve A of Fig. 3, according to models I and II.

Subject to certain approximations, the lattice contribution to the electric field gradient at the Fe nucleus may be deduced from the Co^{59} NMR measurements of Sugawara[23] in the isomorphic cobaltic salt. We assume that in this low spin d_ϵ^6 complex the d electrons maintain cubic symmetry and that only a lattice contribution, modified by the appropriate shielding factor is present. Assuming that the distribution of lattice charge outside the transition metal ion is the same for both salts, the lattice contributions to the EFG at the nuclei are in the ratio of the lattice shielding factors. Using $(1-\gamma_\infty)_{Fe}=10.0$ and $(1-\gamma_\infty)_{Co}=8.0$,[29] we find the lattice contribution to the EFG at the nucleus as given in column 2 of Table IV. This lattice contribution, when added to the valence contribution, yields the net quadrupole splitting shown in curves B_I and B_{II} of Fig. 3. The sign of the lattice EFG is not determined by NMR and we make the choice to give best agreement with our data.

In addition to ΔE we wish to explain the angle and temperature dependence of the single-crystal absorption peak area ratios (Fig. 6). As demonstrated by Zory,[31] the orientation of the EFG relative to the crystal axes can be determined using the Mössbauer spectra of single-crystal samples. Zory has shown [and the application of Eqs. (6) and (15) confirms] that the ratio of the intensities of the two quadrupole peaks in the case of Fe^{57} is given by $R=P_1/P_3$ (assuming the recoil-free fraction to be isotropic), where

$$P_1=\sum_{\text{sites}}\{4(1+\eta^2/3)^{1/2}-[3\cos^2\theta_i-1+\eta\sin^2\theta_i\cos(2\phi_i)]\}, \quad (16)$$

$$P_3=\sum_{\text{sites}}\{4(1+\eta^2/3)^{1/2}+[3\cos^2\theta_i-1+\eta\sin^2\theta_i\cos(2\phi_i)]\},$$

with θ_i and ϕ_i the angles the γ beam makes with the principal axes of the EFG tensor for the ith site. The definitions of θ and ϕ are related to the definition of η in the usual way, and we use the coordinate system in Fig. 1. The sum is over the two different iron sites in the unit cell. The total EFG as calculated above would give rise to the predicted single-crystal peak area ratios under models I and II in Table III. The temperature dependence, which results from the variation in the valence electron contribution, is very small below 77°K

[31] P. Zory, Phys. Rev. 140, A1401 (1965).

TABLE IV. Electric field gradient in $K_3Fe(CN)_6$.

Valence EFG(0°K) (10^{24} cm^{-3})	Lattice EFG[a] (10^{+24} cm^{-3})	Total EFG(0°K) (10^{24} cm^{-3})	Experimental EFG (from area ratios)	
Model I (II)		Model I (II)	(20°)	(300°)
$\frac{V_{xx}}{e}$ +1.60(0.91)	+0.08	+1.68(+0.99)	+0.47	+0.396
$\frac{V_{yy}}{e}$ −2.56(−2.48)	+0.57	−1.99(−1.91)	−1.89	−0.13
$\frac{V_{zz}}{e}$ +0.96(+1.57)	−0.65	+0.31(+0.92)	+1.42	+0.63
Includes factor of $(1-R)=0.68$	Includes factor of $(1-\gamma_\infty)=10.0$ Sign is chosen to give best fit to Mössbauer expt		z axis is 30° from b axis	z axis is 25° from b axis
$\eta=(V_{xx}-V_{yy})/V_{zz}$		11.8(3.15)	1.67	2.26
$\Delta E=\frac{1}{2}eQV_{zz}(1+\eta^2/3)^{1/2}$ (mm/sec)		0.58(0.515)	0.53	0.28

[a] Reference 23.

and we show only the $T=0$°K values for comparison with the 20 and 77°K data in Table III. The calculated area ratios were corrected for the finite thickness of the the absorber corresponding to an effective thickness of 3.5 for a 0.010-in.-thick slice. These calculated values may then be compared to the experimental area ratios.

For an additional comparison to the data we have treated the EFG components as free parameters. The values shown in column 4 of Table IV correspond to the the best fit to the peak area ratios, and give the quadrupole splitting exactly.

At 300°, no satisfactory fit could be found with $\hat{z}\cdot\hat{b}=\cos 30°$ (see Fig. 1). This rotation of the EFG tensor, if real, could result from anisotropic thermal expansion. It is worth noting that from the area-ratio experiments and the single-crystal measurements in a large field the largest component of the EFG is negative and lies along the y axis. This is a characteristic of both models I and II. The role of the 45° rotation of the rhombic field is essential; without it both models would have the large component lying in the x direction.

The agreement between theory and the low-temperature quadrupole spectra is fairly satisfactory. The general trends in the area ratios with temperature and orientation are reproduced, model II doing somewhat better than model I. The quadrupole splitting without free parameters is close to experiment (see Table III), considering the uncertainties which are inherent in the method.

At higher temperatures the situation is less satisfactory, for none of the theoretical curves reproduces the variation of ΔE. There are several relevant experimental facts to consider. The crossover which occurs in the a- and b-axis susceptibilities[8] of the concentrated salt is not predicted by our models. The anomalies at 130°K in the susceptibility[2] and in the specific heat[1] suggest a magnetic transition. It is not known whether the dilute material exhibits these same characteristics. The difference in ΔE between concentrated and dilute material at high temperature may be relevant, especially in view of the observation that the dilute material more nearly follows the prediction (see Fig. 3). The fact that dilute and concentrated samples differ *above* the "transition temperature" is inconsistent with the notion that spin ordering is involved. A neutron-diffraction or x-ray study of this material over a range of temperatures would probably be illuminating.

A very small difference in the peak intensities of powder specimens was observed. The ratio of low-energy peak intensity to that of the high-energy peak varied monotonically from 1.01 to 1.03 in the ranqe 4.2–300°K. This may be evidence of a "Goldanskii" effect.[32]

In samples of $K_3Fe(CN)_6$ and $(NH_4)_3Fe(CN)_6$ dissolved in glycerine, ΔE(77°K) was found to be 0.90 mm/sec, compared to 0.47 mm/sec in the crystalline ferricyanide. This means that the distortion of the complex is different in the solution and probably reflects a small difference in the d-electron wave functions in addition to a modified "lattice" contribution.

The linewidths of some of the measured spectra are shown in Fig. 4. No corrections have been made for absorber thickness, but the plot may be examined for trends in individual samples. In general linewidth increases as temperature is lowered, and appears to rise most rapidly in the region between 130 and 70°K. This may be connected with the specific heat and susceptibility anomalies. More likely, it reflects the magnetic hyperfine interaction made detectable by a reduced spin-lattice relaxation rate. This would explain the levelling off of the curve in the concentrated samples, for further reduction in spin-lattice relaxation will not be effective once the spin-spin relaxation becomes dominant. In the dilute material the broadening con-

[32] V. I. Goldanskii, Phys. Rev. Letters **14**, 769 (1965).

tinues to increase, finally giving rise to the wide low-temperature magnetic hyperfine spectrum.

The isomer shift of various samples of $K_3Fe(CN)_6$ relative to Fe metal as a function of temperature is shown in Fig. 5. We do not attempt to calculate its absolute value, but merely make the comment that it is typical of covalent ferric materials. By virtue of the second-order relativistic Doppler shift, the isomer shift is expected to vary with temperature as $\delta=\langle v^2\rangle_{av}/2c^2 \times(14.4\text{ keV})$, where $\langle v^2\rangle_{av}$ is the average square velocity of the iron atom at temperature T. If we assume equipartititon of thermal energy, then the isomer shift is given by

$$\delta=\frac{U}{2c^2}(14.4\text{ keV}) \quad \text{or} \quad \frac{\partial\delta}{\partial T}=\frac{C_L}{2c^2}(14.4\text{ keV}), \quad (17)$$

where C_L is the lattice specific heat per atom of the salt. In the high-temperature or classical limit of Dulong and Petit, this corresponds to an isomer shift change of -7.3×10^{-4} mm/sec C°, as shown in curve A of Fig. 5. At lower temperatures, quantum effects reduce the rate of change of isomer shift. Curve B has been calculated by using relation (17) and numerically integrating the experimental specific heat.[1] Although the data have a large spread, curve B is clearly preferable. To within the accuracy of the data, no evidence is seen of effects of the anomalies discussed above.

B. Paramagnetic Hyperfine Spectra

When the paramagnetic iron sites are sufficiently separated from each other and are in a low-temperature environment, the spin-spin and spin-lattice relaxation rates become less than the rate of precession of the nucleus in the magnetic field of the electron (about 10^8–10^9/sec in our case). Under these circumstances the nucleus can follow the electron spin and well-defined states exist whose energies depend upon the relative orientation of nuclear and electronic spin. These states give rise to structure in the Mössbauer spectra, with energy splittings equivalent to fields of several hundred kilogauss. This phenomenon has been observed by several workers in a variety of substances[26,33] but we believe that this is the only time it has been seen for a spin-$\frac{1}{2}$ paramagnet with the exception of the hemoglobins.[26]

The effect is clearly seen in Figs. 7 and 8 where decreasing temperature and the concentration decreases the relaxation rate and causes the spectrum to become wide. In principle, one can calculate the development of the magnetic structure as a function of the electronic relaxation time[34] if the hyperfine interactions are known.

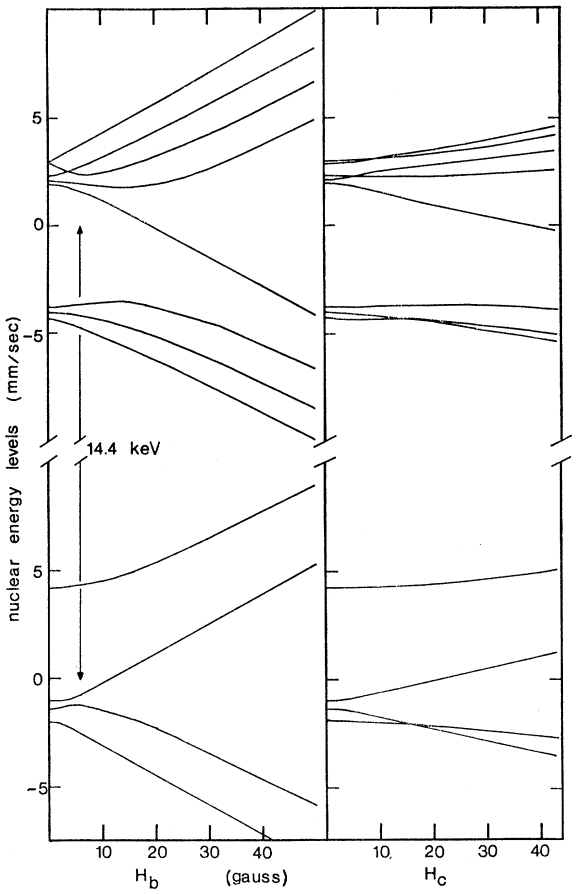

FIG. 13. The energy levels of the Fe^{57} ground and excited states in $K_3Fe(CN)_6$ as a function of external magnetic fields along the crystalline b axis (H_b) and c axis (H_c). The splitting of the levels due to the field along the z axis (H_a) is very similar to that of H_b with the exception that the levels which cross for H_b repel each other for H_a.

However, for an anisotropic interaction in which the nuclear spin states are not pure, this is a very difficult calculation, and we will not attempt it here.

Using the electronic wave functions (5) we can calculate the spectrum in the limit of zero relaxation rate. We have done this for models I and II in zero external field using the Hamiltonian (13), the lattice EFG of column 2, Table IV. The covalency parameter $N^2=0.69$ was chosen to scale the calculated spectrum and a linewidth of 0.60 mm/sec was then folded into the spectrum to represent roughly the effects of relaxation, and the net predicted spectra are the solid curves of Fig. 9(a). Both of these single-parameter calculations are in satisfactory agreement with the data. The peaks at 0.0 mm/sec are definitely not impurity Fe [such as $K_4Fe(CN)_6\cdot 3H_2O$] for they disappear steadily as the concentration and temperature are lowered (Figs. 7 and 8), and also as the magnetic field is increased. The spectrum of the most dilute sample [Fig. 8, 0.33% Fe in $K_3Co(CN)_6$] at

[33] L. E. Campbell and S. De Benedetti, Phys. Letters **20**, 102 (1966); F. E. Obenshain *et al.*, Phys. Rev. Letters **14**, 365 (1965); H. H. Wickman and A. U. Trozzolo, *ibid.* **15**, 156 (1965); H. H. Wickman and G. K. Wertheim, Phys. Rev. **148**, 211 (1966).

[34] E. Bradford and W. Marshall, Proc. Phys. Soc. (London) **87**, 731 (1966); M. Blume and A. J. Tjon, Phys. Rev. (to be published); H. H. Wickman, *Mössbauer Effect Methodology* (Plenum Press, Inc., New York, 1966), Vol. 2, p. 39.

4.2°K shows the nearest approach to the calculated spectrum (solid curve).

In the case of zero external field, the total angular momentum F and F_z as obtained by vector coupling of the nuclear spin $\mathbf{I}$ and the effective electronic spin $\mathbf{S}_{\text{eff}}$ are nearly good quantum numbers. For Fe^{57} in $K_3Fe(CN)_6$, the nuclear spins $\mathbf{I}_{ex}=\frac{3}{2}$ and $\mathbf{I}_{gd}=\frac{1}{2}$ couple to the electronic moment represented by an effective spin of $\mathbf{S}_{\text{eff}}=\frac{1}{2}$ for the low-spin ferric ion. The multiplets $F_{ex}=2$, 1 and $F_{gd}=1$, 0 are thus formed as shown for $\mathbf{H}_{ext}=0$ in Fig. 13. There is a small zero-field splitting due to the anisotropy of the hyperfine interactions.

When the external field strength is increased these multiplets split until the coupling between the nuclear and electronic moments is broken leaving I, I_z and S_{eff}, S_{eff_z} as the good quantum numbers. This is somewhat analogous to the Paschen-Back effect in atomic physics where the coupling between the electronic spin and orbital angular momentum is broken with a strong magnetic field. In the present case the Paschen-Back limit is achieved for external fields large compared to 10 G which is the order of the effective nuclear field acting on the electron.

This effect was predicted by Wickman and Wertheim[33] for the $S_z=\pm\frac{1}{2}$ state of Fe^{3+} in corundum, but they did not observe the effect in the high-spin ferric ion.

Figure 10 shows the development of the Mössbauer spectra of a powder sample of K_3Fe, $Co(CN)_6$ with increasing strength of an external magnetic field parallel to the γ beam. The solid curves in the figure are calculated, using model II and Eq. (13) with no new parameters. The agreement of theory with experiment is seen to be quite good with the exception of the unresolved doublet at 0.0 mm/sec. This is the result of spin-spin relaxation which disappears with further dilution (see Fig. 8).

The spectra of Figs. 9(b) and 9(c) were observed in fields sufficiently strong to decouple the nuclear and electronic spins. The solid curves are the result of calculations based on models I and II with magnetic fields parallel and perpendicular to the direction of incidence of the γ beam. One can observe the difference between models I and II in these calculations—model II is clearly preferable here.

Data taken in applied fields with $K_3Fe(CN)_6$ dissolved in glycerine give results very similar to the spectra of solid K_3Fe, $Co(CN)_6$ (Fig. 9). The much broader absorption lines in the glycerine may be due to a heterogeneous environment.

Spectra of Figs. 11(a), 11(b), and 11(c) were taken for single crystals of concentrated $K_3Fe(CN)_6$ in large magnetic fields and very low temperatures. The electron-spin relaxation is very fast between the two members of the ground-state Kramers doublet, and the magnetic interaction is proportional to the magnetization as discussed earlier. The relative strengths of effective magnetic field in the three cases agree well with model II.

Because the magnetic hyperfine interaction is strong it determines the nuclear quantization axis and the quadrupole shift of lines 1 and 6 relative to 2, 3, 4, and 5 is a measure of the field gradient along this axis. The observed field gradients are in good agreement with model II.

6. SUMMARY

Mössbauer spectra of the ferricyanide complex have been observed in a variety of situations and have been compared with calculations using parameters found by other methods. Only the covalency parameter has been adjusted to fit the present data. The value $N^2=0.69$ has been determined from the strength of the magnetic hyperfine interaction. The two models which have been considered differ by a rotation of the rhombic field through 90° about the crystalline c axis. Model I corresponds to the arrangement found in ESR measurements of the magnetically dilute isomorphous $K_3(Fe,Co)(CN)_6$,[7,35] while model II employs the same values deployed as suggested by the ESR signals and susceptibility measurements from the concentrated salt. Model II is consistent with all of the Mössbauer spectra observed at or below 77°K. In particular, it is clearly preferable to model I in the dilute material where the latter might be expected to hold. The data for temperatures which would correspond to significant electronic thermal excitation are not consistent with either model, and it appears that a temperature-dependent crystal field must be invoked to account for the observed quadrupole splitting.

ACKNOWLEDGMENTS

The authors take particular pleasure in thanking Professor S. De Benedetti for advice and help in the present work and for continuing inspiration. Thanks are also due to Professor R. B. Griffiths and Professor S. A. Friedberg for helpful discussion in the course of this work, to Professor P. A. Flinn and Dr. B. S. Window for the use of their curve-fitting programs, and to Dr. F. De S. Barros for help with some of the data collection. We are also grateful to Dr. Roger J. Anderson for remeasuring the g tensor of Fe in $K_3Co(CN)_6$, to Dr. Larry Epstein for advice on chemical preparation, and to S. A. Wilson for orienting a single crystal. One of us (W.T.O.) wishes to thank the National Science Foundation for the support of a postdoctoral fellowship during part of this work.

APPENDIX

We now determine the matrix elements of the g tensor, electric-field-gradient tensor, and the magnetic hyperfine tensor in a very pedestrian but straight-

[35] R. J. Anderson (private communication).

forward way. These matrix elements are calculated within the ground-state Kramers doublet defined in (5) and can always be extended to include the higher excited states by the appropriate Boltzmann averages. It is convenient to treat the hyperfine interaction problem in terms of operators in the x, y, z system, the system in which the g tensor is diagonal. It is conceptually simple however, to do the various integrations over hole coordinates in the x', y', z' system and that is the procedure which we follow.

We can express the states $|+\rangle$ and $|-\rangle$ as defined by (4), in terms of x', y', z' by using (1) and (2). Operators in the system (x,y,z) are also transformed to the cubic system so that the calculations can be done by using wave functions and operators expressed in the same coordinates.

An operator evaluated between states of the form $|S_z, I_z\rangle$ can be separated into nuclear and electronic parts: $\langle S_z'|O_e|S_z\rangle\langle I_z'|O_n|I_z\rangle$. The nuclear part is easily found since it involves only the nuclear spin operators I_x, I_y, I_z. The electronic part is more complicated.

To calculate the electronic part of the matrix element, we first expand the wave functions in terms of $|a\rangle$, $|b\rangle$, and $|c\rangle$. For example,

$$\begin{aligned}\langle+|O|+\rangle=a^2\langle a\alpha|O|a\alpha\rangle+ab\langle a\alpha|O|b\beta\rangle+iac\langle a\alpha|O|c\beta\rangle\\+ab\langle b\beta|O|a\alpha\rangle+b^2\langle b\beta|O|b\beta\rangle+ibc\langle b\beta|O|c\beta\rangle\\-iac\langle c\beta|O|a\alpha\rangle-ibc\langle c\beta|O|b\beta\rangle+c^2\langle c\beta|O|c\beta\rangle.\end{aligned}\quad(18)$$

After examining the nature of the operator O we can decide which of these matrix elements are zero by orthogonality, selection rules, or by symmetry, and which must be calculated. Each of the nonzero elements above must in turn be expanded if the operator involves the coordinates of the electron. For example, if $O=Y_2'^{\pm2}$, then

$$\begin{aligned}\langle b\beta|Y_2'^{\pm2}|b\beta\rangle=l_{xz}^2\langle x'y'|Y_2'^{\pm2}|x'y'\rangle+l_{xz}l_{xx}\langle x'y'|Y_2'^{\pm2}|y'z'\rangle+l_{xz}l_{xy}\langle x'y'|Y_2'^{\pm2}|x'z'\rangle+l_{xx}l_{xz}\langle y'z'|Y_2'^{\pm2}|x'y'\rangle\\+l_{xx}^2\langle y'z'|Y_2'^{\pm2}|y'z'\rangle+l_{xx}l_{xy}\langle y'z'|Y_2'^{\pm2}|x'z'\rangle+l_{xy}l_{xz}\langle x'z'|Y_2'^{\pm2}|x'y'\rangle+l_{xy}l_{xx}\langle x'z'|Y_2'^{\pm2}|y'z'\rangle\\+l_{xy}^2\langle x'z'|Y_2'^{\pm2}|x'z'\rangle=(l_{xy}^2-l_{xx}^2\pm2il_{xy}l_{xx})\tfrac{1}{2}[(\sqrt{6})/7](5/4\pi)^{1/2}=-\tfrac{1}{2}[(\sqrt{6})/7](5/4\pi)^{1/2}e^{\mp2i\gamma},\end{aligned}\quad(19)$$

where in the last step we specialize to a rotation about z by γ.

A. g Tensor

To calculate the matrix elements of the g tensor, we make use of the relation $\mathbf{H}\cdot(\mathbf{L}+2\mathbf{S})=\mathbf{H}\cdot\tilde{g}\cdot\mathbf{S}_{\text{eff}}$ or $kL_i+2S_i=\sum_j g_{ij}S_{\text{eff}\,j}$. We find from Eqs. (3) and (4) that $\langle+|L_i|+\rangle=-2bc\delta_{iz}$ and $\langle+|L_i|-\rangle=2ac\delta_{iz}-2iab\delta_{iy}$. It is also easy to find $\langle+|S_i|+\rangle=\frac{1}{2}(a^2-b^2-c^2)\delta_{iz}$ and $\langle+|S_i|-\rangle=\frac{1}{2}(a^2-b^2+c^2)\delta_{iz}-(i/2)(a^2+b^2-c^2)\delta_{iy}$. The effective spin operator $\mathbf{S}_{\text{eff}}$ is defined by its nonzero matrix elements $\langle\pm|S_{\text{eff}i}|\pm\rangle=\pm\frac{1}{2}\delta_{iz}$ and $\langle\pm|S_{\text{eff}i}|\mp\rangle=\frac{1}{2}\delta_{ix}\mp(i/2)\delta_{iy}$. Thus we have

$$\langle+|L_i+2S_i|+\rangle=\langle+|\textstyle\sum_j g_{ij}S_{\text{eff}i}|+\rangle=\sum_j g_{ij}\langle+|S_{\text{eff}i}|+\rangle=\tfrac{1}{2}g_{iz}=k(-2bc\delta_{iz})+2(\tfrac{1}{2})(a^2-b^2-c^2)\delta_{iz}.\quad(20)$$

Therefore, $g_{iz}=2(a^2-b^2-c^2-2kbc)\delta_{iz}$. When the real and imaginary parts are equated we obtain the following expressions:

$$g_{ix}=2(a^2-b^2+c^2+2kac)\delta_{ix},\quad g_{iy}=2(a^2+b^2-c^2+2kab)\delta_{iy}.\quad(21)$$

B. Quadrupole Interaction

In general, the quadrupole interaction may be written as[36]

$$\mathcal{H}_Q=eQ/4I(2I-1)\{V_{zz}[3I_z^2-I(I+1)]+V_1(I_-I_z+I_zI_-)+V_{-1}(I_+I_z+I_zI_+)+V_{-2}I_+^2+V_2I_-^2\},\quad(22)$$

where $V_{\pm1}=V_{xz}\pm iV_{zy}$, and $V_{\pm2}=\frac{1}{2}(V_{xx}-V_{yy})\pm iV_{xy}$. In the principal axis system of the EFG, $V_{xy}=V_{zx}=V_{zy}=0$. However, in the axis system rotated by γ about the z axis $V_{xy}\neq V_{zx}=V_{zy}=0$. Thus for $K_3Fe(CN)_6$ with $I=\frac{3}{2}$, we have the following expression for the quadrupole interaction in the x, y, z system:

$$\mathcal{H}_Q=eQ/4[V_{zz}(I_z^2-5/4)+I_+^2(V_{xx}-V_{yy}-2iV_{xy})/6+I_-^2(V_{xx}-V_{yy}+2iV_{xy})/6].\quad(23)$$

Thus, we need to find matrix elements of the form

$$q=V_{zz}/e=(3z^2-r^2)/r^5=(16\pi/5)^{1/2}Y_2^0\langle r^{-3}\rangle N^2\quad(24)$$

and $\tau_\pm=(V_{xx}-V_{yy}\pm2iV_{xy})/e=3(x^2-y^2\pm2ixy)/r^5=3(32\pi/15)^{1/2}Y_2^{\pm2}\langle r^{-3}\rangle N^2$. We can express these operators in the x', y', z' system as $Y_2^0=Y_2'^0$ and $Y_2^{\pm2}=Y_2'^{\pm2}e^{\mp2i\gamma}$. Therefore,

$$\begin{aligned}\langle+_\eta|Y_2^0|+_\eta\rangle=\langle-_\eta|Y_2^0|-_\eta\rangle=\{a_\eta^2[-2l_{zz}^2/7+(l_{zy}^2+l_{zx}^2)/7]+b_\eta^2[-2l_{xz}^2/7+(l_{xy}^2+l_{xx}^2)/7]\\+c_\eta^2[-2l_{yz}^2/7+(l_{yy}^2+l_{yx}^2)/7]\}(5/4\pi)^{1/2}=\{-2a_\eta^2/7+(b_\eta^2+c_\eta^2)/7\}(5/4\pi)^{1/2}.\end{aligned}\quad(25)$$

[36] M. H. Cohen and F. Reif, Solid State Phys. 5, 321 (1957).

So

$$q_{\rm val}=V_{zz}/e=\{-4a_\eta^2/7+2(b_\eta^2+c_\eta^2)/7\}\langle r^{-3}\rangle N^2,$$

$$\begin{aligned}\langle+_\eta|Y_2^{\pm2}|+_\eta\rangle&=\langle-_\eta|Y_2^{\pm2}|-_\eta\rangle=\langle+_\eta|Y_2'^{\pm2}e^{\mp2i\gamma}|+_\eta\rangle\\&=\{a_\eta^2[l_{xy}^2-l_{xx}^2\pm2il_{xy}l_{xx}]+b_\eta^2[l_{xy}^2-l_{xx}^2\pm2il_{xy}l_{xx}]+c_\eta^2[l_{yy}^2-l_{yx}^2\pm2il_{yy}l_{yx}]\\&+b_\eta ic_\eta[l_{xy}l_{yy}-l_{xx}l_{yx}\pm i(l_{xy}l_{yx}+l_{xx}l_{yy})]-b_\eta ic_\eta[l_{xy}l_{yy}-l_{xx}l_{yx}\pm i(l_{yx}l_{yx}+l_{xx}l_{yy})]\}e^{\mp2i\gamma}\cdot\tfrac{1}{2}[(\sqrt{6})/7](5/4\pi)^{1/2}\\&=(c_\eta^2-b_\eta^2)e^{\mp4i\gamma}\tfrac{1}{2}[(\sqrt{6})/7](5/4\pi)^{1/2};\end{aligned}\tag{26}$$

therefore, $\tau_\pm=(V_{xx}-V_{yy}\pm2iV_{xy})/e=(6/7)(c_\eta^2-b_\eta^2)\langle r^{-3}\rangle N^2e^{\mp4i\gamma}$. A comparison of (23), (26), and (8) verifies our earlier statement about the quadrupole Hamiltonian in the xyz system. We see that the transformation to x, y, z involves multiplying ηq in the upper triangle of H_Q by $e^{i4\gamma}$, while the lower triangle contains the complex conjugate.

C. Magnetic Hyperfine Interaction

The magnetic hyperfine interaction $\mathcal{H}_M$ is written in Eq. (9) and can be expanded in the following way:

$$\begin{aligned}\mathcal{H}_M=P\{&I_zL_z+\tfrac{1}{2}(I_+L_-+I_-L_+)-(1+\kappa)[I_zS_z+\tfrac{1}{2}(I_+S_-+I_-S_+)]\\&+3[S_zI_zz^2/r^2+\tfrac{1}{2}(S_+I_-+S_-I_+)(x^2+y^2)/r^2+\tfrac{1}{4}S_+I_+(32\pi/15)^{1/2}Y_2^{-2}\\&+\tfrac{1}{4}S_-I_-(32\pi/15)^{1/2}Y_2^{2}+\tfrac{1}{2}(S_zI_++S_+I_z)(8\pi/15)^{1/2}Y_2^{-1}-\tfrac{1}{2}(S_zI_-+S_-I_z)(8\pi/15)^{1/2}Y_2^{1}]\}.\end{aligned}\tag{27}$$

Since we wish to express the coordinates in the x', y', z' system, we use $z=z'$, $x=x'\cos\gamma+y'\sin\gamma$, $y=y'\cos\gamma-x'\sin\gamma$ to obtain the following equation:

$$\begin{aligned}\mathcal{H}_M=P\{&I_zL_z+\tfrac{1}{2}(I_+L_-+I_-L_+)-(1+\kappa)[I_zS_z+\tfrac{1}{2}(I_+S_-+I_-S_+)]\\&+3[S_zI_zz'^2/r^2+\tfrac{1}{4}(S_+I_-+S_-I_+)(x'^2+y'^2)/r^2+\tfrac{1}{4}S_+I_+(32\pi/15)^{1/2}Y_2'^{-2}e^{+2i\gamma}\\&+\tfrac{1}{4}S_-I_-(32\pi/15)^{1/2}Y_2'^{2}e^{-2i\gamma}+\tfrac{1}{2}(S_zI_++S_+I_z)(8\pi/15)^{1/2}Y_2'^{-1}e^{i\gamma}-\tfrac{1}{2}(S_zI_-+S_-I_z)(8\pi/15)^{1/2}Y_2'^{+1}e^{-i\gamma}]\}.\end{aligned}\tag{28}$$

Using the procedure outlined above, the matrix elements $\langle S_z'I_z'|\mathcal{H}_M|S_zI_z\rangle$ may be calculated. Of the last four terms the only nonzero contributions are in $\langle+,-\frac{1}{2}|\mathcal{H}_M|-,+\frac{1}{2}\rangle$ and $\langle+,+\frac{1}{2}|\mathcal{H}_M|-,-\frac{1}{2}\rangle$ and their complex conjugates (for the nuclear gd state where $I=\frac{1}{2}$):

$$\begin{aligned}\langle+,-\tfrac{1}{2}|\mathcal{H}_M|-,+\tfrac{1}{2}\rangle=P\langle+|&\tfrac{1}{2}L_+-(3S_+/4)(x'^2+y'^2)/r^2+(3S_-/4)(32\pi/15)^{1/2}Y_2'^2e^{-2i\gamma}\\&-(1+\kappa)(S_z/2)-(3S_z/2)(8\pi/15)^{1/2}Y_2'^1e^{-i\gamma}|-\rangle\langle-\tfrac{1}{2}|I_-|+\tfrac{1}{2}\rangle.\end{aligned}\tag{29}$$

We have found previously that

$$\begin{aligned}\langle+|L_+|-\rangle&=\langle+|L_x+iL_y|-\rangle=2a(b+c),\\\langle+|S_+|-\rangle&=\langle+|S_x+iS_y|-\rangle=a^2,\\\langle+|Y_2'^2S_-|-\rangle&=-b^2\langle b|Y_2'^2|b\rangle+c^2\langle c|Y_2'^2|c\rangle+bic\langle c|Y_2'^2|b\rangle+bic\langle b|Y_2'^2|c\rangle\\&=-b^2\{-\tfrac{1}{2}[(\sqrt{6})/7](5/4\pi)^{1/2}e^{-2i\gamma}\}+c^2\{+\tfrac{1}{2}[(\sqrt{6})/7](5/4\pi)^{1/2}e^{-2i\gamma}\}\\&+2bic\{l_{xy}l_{yy}-l_{xx}l_{yx}+i(l_{xy}l_{yx}+l_{yy}l_{xx})\}\tfrac{1}{2}[(\sqrt{6})/7](5/4\pi)^{1/2}=(c-b)^2e^{-2i\gamma}\tfrac{1}{2}[(\sqrt{6})/7](5/4\pi)^{1/2},\\\langle+|S_+[(x'^2+y'^2)/r^2]|-\rangle&=a^2\langle a|[(x'^2+y'^2)/r^2]|a\rangle=a^2\{(6/7)l_{zz}^2+(4/7)(l_{xz}^2+l_{yz}^2)\}=(6/7)a^2,\\\langle+|Y_2'^1S_z|-\rangle&=\tfrac{1}{2}\{-ab\langle a|Y_2'^1|b\rangle+aic\langle a|Y_2'^1|c\rangle-ab\langle b|Y_2'^1|a\rangle+aic\langle c|Y_2'^1|a\rangle\}\\&=\tfrac{1}{2}\{-2ab[-(1/14)(15/2\pi)^{1/2}e^{i\gamma}]+2aic[-(1/14)(15/2\pi)^{1/2}e^{i\gamma}]\},\\\langle+,-\tfrac{1}{2}|\mathcal{H}_M|-,+\tfrac{1}{2}\rangle&=P\{a(b+c)-(1+\kappa)\tfrac{1}{2}a^2+(3/14)(c-b)^2e^{-4i\gamma}+(9a^2/14)-3a(b+c)/14\}.\end{aligned}\tag{30}$$

If we compare this matrix element with the matrix element $\langle+,-\frac{1}{2}|\mathbf{I}\cdot\tilde{A}\cdot\mathbf{S}_{\rm eff}|-,+\frac{1}{2}\rangle$ we can make the identification of

$$\tfrac{1}{4}(A_x+A_y+2iC_{xy})=P\{a(b+c)-(1+\kappa)\tfrac{1}{2}a^2+(3/14)(c-b)^2e^{-4i\gamma}+(9a^2/14)-3a(b+c)/14\},\tag{31}$$

where $C_{xy}=P[3(c-b)^2/7]\sin4\gamma$ which arises because of the monoclinic symmetry.